A Collider Search for Dark Matter Produced in Association
with a Higgs Boson with the CMS Detector at the 13 TeV LHC

By

Dustin Ray Burns
B.S. Physics (Georgia Institute of Technology) 2011
B.S. Applied Mathematics (Georgia Institute of Technology) 2011
M.S. Physics (University of California, Davis) 2012

Dissertation

Submitted in partial satisfaction of the requirements for the degree of

Doctor of Philosophy

in

Physics

in the

Office of Graduate Studies

of the

University of California

Davis

Approved:

_____

Chair Michael Mulhearn

_____

Robin Erbacher

_____

Albert De Roeck

Committee in Charge

2017

To someone very important . . .

a nice dedication.

CONTENTS

LIST OF FIGURES

LIST OF TABLES

ABSTRACT

**A Collider Search for Dark Matter Produced in Association
with a Higgs Boson with the CMS Detector at the 13 TeV LHC**

The abstract submitted as part of your dissertation, in the introductory pages, does not have a word limit. It should follow the same format as the rest of your dissertation (1.5 inch left margin, double-spaced, consecutive page numbering, etc.).

ACKNOWLEDGMENTS

Acknowledgements to those who helped you get to this point. They should be listed by chapter when appropriate.

Chapter 1

Motivation and theoretical background

The first section of this chapter lays the theoretical framework of the Standard Model (SM) of particle physics, including the historical discovery timeline of symmetries of nature, each corresponding to a leap forward in our physical understanding, and the model's particle content and their properties. The second section extends the symmetry group of the SM to include candidates for the observed cosmic dark matter (DM) and the particles that could mediate the DM-SM interactions.

1.1   The Standard Model

1.1.1   Symmetries of nature

Each major advance in the history of physics has corresponded to the discovery and mathematical implementation of a new global space-time, global discrete, or local gauge symmetry. In this section, I will review these discoveries, informally developing the mathematical framework needed to understand the symmetry groups of the SM. Along the way, two important subplots will play out: the development of our understanding of physics at smaller distance scales and higher energies, and the unification of previously separate physical sectors.

Our ancient ancestors were aware that certain geometrical shapes, e.g. the Platonic solids, possessed the quality of symmetry, and were driven to understand the composition

of physical substances by breaking them down into fundamental, indivisible units. These units, known as atoms by the ancient Greeks, interact and rearrange themselves according to physical laws to account for the variety of substances and physical phenomena we observe. The attraction to applying symmetry to nature is evidenced by the centuries-long belief that the Earth lie at the center of the universe, with the celestial bodies orbiting in perfect, divine circles.

The end of the scientifically repressive middle ages brought along an improvement in astronomical observations and the growth of the pseudo-scientific field of alchemy, which attempted to reduce, understand, and manipulate the fundamental elements of physical substances. When Kepler discovered three laws of planetary motion, he unified the description of the motion of the planets. For the first time, the conservation of a physical quantity, what we now know as angular momentum, was associated with a general set of physical objects. At the burgeoning of the scientific revolution, Newton championed the idea that the same physical laws can be applied to all physical events, and that properties of these laws can be abstracted to apply to nature at a fundamental level.

Newton defined an inertial reference frame implicitly as one where his first law held, that is, that an object remains at constant motion unless acted on by an outside force. Since his laws were the same in all inertial reference frames, a new symmetry of nature was discovered, now called symmetry under Euclidean transformations. Since Euclidean transformations form a mathematical group, it is said that classical mechanics is invariant under the Euclidean group. The invariance under the Euclidean transformations can be used to derive conservation laws: Newton's laws don't depend on spatial translations or rotations, implying the conservation of linear and angular momentum, respectively. These relationships foreshadow Noether's abstraction of the connection between continuous symmetries and conserved quantities. She proved that there is a conserved quantity, or current, associated with every symmetry of a physical system [**?**]. This famous theorem facilitates the derivation of conserved quantities and will be used extensively in the theories that follow. The extension of the Euclidean transformations to include time

translations and motion at constant velocity (boosts) forms the Galilean group.

The next symmetry of nature to be discovered came when Lorentz found that Maxwell's equations, which unified the classical eletricity and magnetism sectors [?], were invariant under a set of transformations that generalized the classical Galiliean translations, now called Lorentz transformations, which form the Lorentz group [?]. The Lorentz symmetry corresponds to the conservation law of total electric charge [?]. Soon after, Einstein derived the Lorentz symmetry as a property of space-time itself through his special theory of relativity, assuming two simple postulates: the laws of physics and the speed of light are the same in all inertial reference frames [?]. From these simple assumptions, Einstein was able to extend the classical laws of physics to the high velocity, high energy sector. Before Einstein, the symmetries of nature were thought to be consequences of the physical laws themselves, but Einstein's major paradigm shift was to view the symmetry itself as the more fundamental property, an insight key to his formulation of the general theory of relativity for the gravitational interaction [?], which is not discussed further in this thesis. Combining the Lorentz and Euclidean transformations yields the Poincare group, the final global space-time symmetry of the SM.

Just as relativists were probing physics at higher speeds and energies, other physicists were investigating the behavior of systems at smaller distance scales, conducting experiments to explore phenomena such as the Compton effect [?] and photoelectric effect[?], which showed the quantized, particle-like behavior of light, and electron beam diffraction [?], which showed the wave-like behavior of electrons. Quantum theory was developed to consolidate the wave-like and particle-like behaviors of systems, and extended the validity of classical physics to microscopic scales. Where in classical physics particles states were described by their absolute position and momentum, quantum theory describes the state of a system by a probabalistic wavefunction. The classical symmetries and conservation laws carried over to quantum theory, with the concept of angular momentum generalized to include spin. Particles with zero or integer spin are called Bosons, and were shown to obey Bose-Einstein statistics, where the wavefunction is symmetric under all permutations of particles. Particles with half-integer spin, called Fermions, obey Fermi-Dirac

statistics, where the wavefunction is symmetric under even permutations and changes sign under odd permutations, implying that no two particles can occupy the same state. These many-particle symmetries were applied to derive properties of materials and states of electrons in atomic and periodic systems, blackbody radiation, and many other properties of matter and radiation [**?**].

Quantum theory was successfully applied to a myriad of low-energy systems. Dirac extended quantum theory and the Schrodinger equation, which describes the evolution of a quantum system in time, to the relativistic regime [**?**]. His formulation of the wave equation for a spin-1/2 particle with mass m is inherently Lorentz invariant:

$$(i\gamma^{\mu}\partial_{\mu} - m)\psi = 0 \tag{1.1}$$

The solutions to the Dirac equation were found to have both positive and negative energy solutions, to the surprise of Dirac. His explanation was that the vacuum consisted of a "sea" of negative energy solutions, each in a distinct state due to the Pauli exclusion principle, and when a pair of electrons was produced, a positive energy state was filled and a negative energy state was vacated, creating a "hole" in the sea. The particle corresponding to this hole would have the same energy as the electron, but in order to conserve total charge, must have the opposite sign charge. This positively charged electron was not know to exist at the time, but was soon discovered in cosmic ray experiments and named the positron [**?**]. Dirac's theoretical prediction of the positron and its subsequent discovery opened the door for the discovery that every particle has an oppositely charged antimatter partner.

In an attempt to apply relativistic quantum theory to the electromagnetic field and the spin-0 photon, Dirac formulated the theory of quantum electrodynamics (QED) [**?**]. QED is the first example of a quantum field theory (QFT), where the physical dynamics apply to the quantum field associated with a particle rather than the particle itself, and particles/antiparticles interact as excitations of the field. This formulation of creation and annihilation of particles and antiparticles gave a more physically intuitive explanation for the negative energy solutions of the Dirac equation than the Dirac sea. QED became the

prototype for developing future relativistic quantum theories and Dirac's procedure the template for quantizing a general field theory.

With the discovery of antimatter and the apparatus of QFT in place, physicists continued searching for additional symmetries. If a particle state is an eigenvector of a symmetry operator, then the eigenvalue is an important quantum number of the state, since if the symmetry is conserved, the quantum number can be used to determine if a decay or interaction of this state is allowed. Three important discrete symmetries operations, and their products, have had significant importance: space coordinate parity inversion (P), particle-antiparticle charge conjugation (C), and time reveral (T) [?]. Violation of P was observed for the weak interactions by Wu and others in the decays of Co-60 atoms [?]. Although it was long believed to be a symmetry of all the interactions, CP, the product of C and P was also found to be violated by the weak decays of K mesons [?]. It is only the combination of P, C, and T that is now thought to be an exact symmetry of nature, obeyed by all interactions. The CPT symmetry was proven to be conserved in all relativistic QFTs [?, ?].

The mid-20th century saw an explosion of discovery in particle physics and was a golden age for the feedback between theoretical and experimental work. The discovery of additional particles such as the muon [?], pion [?], neutrino[?], and many others inspired the theoretical development of the quark model [?], the refinement of QED [?, ?, ?, ?, ?, ?, ?, ?], and the formulation of theories to explain the strong [?, ?, ?, ?, ?] and weak [?] nuclear forces. Conversely, these new theories led to the prediction and subsequent discovery of new fundamental particles, such as the charm [?, ?] and bottom [?] quarks, and composite particles, such as the Ω^- [?].

The development of the theories of the strong and weak forces unveiled a new set of symmetries: local invariance under unitary gauge transformations. In keeping with the trend of the discovery of new symmetries being associated with the unification of physical sectors, the electromagnetic and weak nuclear interactions were found to be components of a single force, called the electroweak force [?, ?]. Again, with QED as the prototype, the Langrangians for the electroweak and strong forces were constructed to

be invariant under unitary groups. Early work by Weyl [**?**] showing the gauge invariance of electromagnetism was extended to QED, and lay the mathematical framework for describing the gauge invariance of the other forces. To demonstrate gauge invariance and how the gauge group generators are asssociated with the force carriers, take the QED terms of the SM Lagrangian as an example case [**?**]:

$$\mathcal{L} \supset \bar{\psi}(i\gamma^\mu D_\mu - m)\psi - \frac{1}{4}F^{\mu\nu}F_{\mu\nu} \tag{1.2}$$

where A_μ is the EM 4-potential and field corresponding to the photon, $F^{\mu\nu} = \partial^\mu A^\nu - \partial^\nu A^\mu$ is the electromagnetic field tensor, and $D_\mu = \partial_\mu + ieA_\mu$ is the gauge covariant derivative. These terms are invariant under the the U(1) transformations

$$\psi \to e^{i\theta(x)}\psi. \tag{1.3}$$

In general, the generators of an interaction's continuous symmetry group correspond to the gauge fields whose excitations are the gauge bosons that mediate that interaction. Just how A_μ is the field corresponding to the photon in QED and generator of the U(1) symmetry group of EM, the W and Z bosons and gluons are formed from the generators of the symmetry groups for the electroweak and strong interactions, SU(2)xU(1) and SU(3), respectively. Additionally, the covariant derivative is transformed in a way analagous to the QED covariant derivative, adding a factor for each generator with the corresponding charge in the coefficient. These charges (electric, color, weak isospin and hypercharge) are conserved for all of the forces in all interactions[**?**]. The charges of the SM particles are described in more detail in the next section.

Although the mathematical descriptions of their symmetries are similar, the EM, weak, and strong nuclear forces are quite different qualitatively. The EM force is the most familiar, being responsible for the interactions of matter and radiation at macroscopic scales, having only one type of charge which can be postitive or negative. The strong force is mediated by eight gluons, corresponding to the eight generators of SU(3), and carries three types of charge, known as red(R), green(G), and blue(B). The "negatives" of these charges are called anticolors: antired($\bar{R}$), antigreen($\bar{G}$), and antiblue($\bar{B}$). Keeping with

the visible color analogy, the theory of the strong force is called quantum chromodynamics (QCD). At low energies, the quarks and antiquarks are confined to form only color-neutral states. This is known as color confinement, and implies no free quarks exist, but only come in neutral combinations called hadrons. Since hadrons are strictly color-neutral, their states transform as the singlet representation under SU(3). At high energies, the strong coupling decreases, and the quarks can be treated as effectively free particles with perturbation theory using Feynman diagrams. This property of the strong force is known as asymptotic freedom. The weak force is qualitatively different than either the EM or strong forces, as particles do not exchange its mediators to form bound states of any kind. The low-energy limit of the weak theory was developed by Fermi to explain beta decays [?], but the full description was not developed until the electroweak force was formulated.

The unification of the electromagnetic and weak interactions into the electroweak force at about 100 GeV had one major shortcoming: the invariance of the Lagrangian required the gauge bosons, B from U(1) and W^1, W^2, W^3 from SU(2), to be massless. While the photon is indeed massless, the W and Z bosons have a nonzero mass []. Higgs and others [?, ?, ?, ?, ?, ?] proposed a solution by introducing a new scalar field whose excitations were called the Higgs boson (H). The scalar field is a complex doublet, meaning it has four total real components, and its vacuum expectation value (vev), or value throughout all of space, is one of many non-zero values in the bottom of its "Mexican hat" potential. This spontaneous symmetry can be broken by choosing one of the values for the vev: $H = \frac{1}{\sqrt{2}}(0, \nu)$, where $\nu = 246$ GeV is called the H vev. At energies above $O(100)$ GeV, the electroweak symmetry is obeyed, the gauge bosons are massless, and the Higgs field has one of many values along the circle at the base of its potential. When the H field is expressed as a perturbation about this vev, the electroweak symmetry is broken into the weak and EM forces, and mass terms are generated for the weak force bosons, which are expressed as linear combinations of B, W^1, W^1, W^3. The process of the Higgs acquiring a vev, spontaneously breaking the symmetry in its potential, and generating the masses of the weak bosons, is know as the Higgs mechanism, and results in the breaking of the electroweak symmetry. This mechanism can be carried out for a general operator

depending on H with the substitution

$$H \rightarrow \frac{1}{2}(\nu + h) \tag{1.4}$$

where h is the physical Higgs, corresponding to the leftover degree of freedom of the H doublet that is not absorbed by the three massive gauge bosons. H couples to the SM fermions, detailed in the next section, not by the same mixing as described for the gauge bosons, but via Yukawa interactions, direct couplings whose coefficients are related the the fermion masses. The Higgs mechanism was the final piece of the puzzle to understanding the fundamental laws of particle physics.

The final result of this saga is the standard model of particle physics, a relativistic gauge quantum field theory, globally invariant under the Poincare group, and locally invariant under the product of the strong and electroweak symmetry groups, SU(3)xSU(2)xU(1), which describes all of the fundamental particles and their interactions. The particle content of the SM is detailed in the next section.

1.1.2   Particle content

The particle content of the SM is displayed in Table 1.1

u	c	t	...	γ	H
d	s	b		g	...
e	μ	τ		W	
ν_e	ν_μ	ν_τ		Z	

Table 1.1: The particles of the Standard Model.

The particles of the standard model consist of the spin-1/2 fermions, which interact to form regular matter, the spin-1 bosons, which mediate the interactions of the fermions, and the spin-0 scalar Higgs boson, which generates the masses of the bosons and fermions via the Higgs mechanism. Unless otherwise labeled, the material in this section comes from [?].

The fermions come in three sets of increasing masses, called generations, correspond-
ing to the first three columns of Table 1.1. Across the rows, the particles have sim-
ilar properties, and are abbreviated u^i, d^i, e^i, ν_e^i from top to bottom with $i = 1, 2, 3$
the generation index. Within each generation, the fermions are divided into two cat-
egories: the quarks, which are charged under the EM, weak, and strong forces, and
the leptons, which are charged under the EM and weak forces. Each fermion has a
corresponding antiparticle, whose mass is the same, but whose charges are opposite
in sign. The quarks are SU(3) triplets, having a color charge of either R, G, or B.
Since the weak force violates P, the fermions can be distinguished by their chirality, be-
ing labelled as either right handed (e_R^i) or left handed (e_L^i). The $(u^i, d^i)_L$ and $(e^i, \nu_e^i)_L$
pairs and their right handed anti-particle pairs are SU(2) doublets and interact via the
weak force. The right handed fermions (left handed anti-fermions) are SU(2) singlets
and do not interact via the weak force. The weak isospins (T_3) for the left handed
fermions are: $(u^i, d^i)_L = (1/2, -1/2)$ and $(e^i, \nu_e^i)_L = (-1/2, 1/2)$. The EM charges are
$(u^i, d^i)_L = (2/3e, -1/3e)$ and $(e^i, \nu_e^i)_L = (-1e, 0)$, and finally, the weak hypercharges are,
from the relation $Y_W = 2(Q - T_3)$, $(u^i, d^i)_L = (1/3, 1/3)$ and $(e^i, \nu_e^i)_L = (-1, -1)$.

The fourth column of Table 1.1 lists the force mediators, or gauge bosons. g stands for
the 8 gluons of QCD that mediate the strong nuclear force. The gluons are octets under
SU(3), and correspond to linear combinations of the generator gauge fields G_μ^a. Gluons
carry color charge themselves, but are electrically neutral. They are massless, consistent
with the fact that they correspond to generators of a conserved symmetry, and may be
represented using the Gell-Mann matrices as the linearly independent set of states [?]:

$$\frac{1}{\sqrt{2}}(r\bar{b}+b\bar{r})\frac{1}{\sqrt{2}}(r\bar{g}+g\bar{r})\frac{1}{\sqrt{2}}(b\bar{g}+g\bar{b})\frac{1}{\sqrt{2}}(r\bar{r}-b\bar{b})-i\frac{1}{\sqrt{2}}(r\bar{b}-b\bar{r})-i\frac{1}{\sqrt{2}}(r\bar{g}-g\bar{r})-i\frac{1}{\sqrt{2}}(b\bar{g}-g\bar{b})\frac{1}{\sqrt{6}}(r\bar{r}+b\bar{b}-2g\bar{g})$$
$$\tag{1.5}$$

while the color singlet state that the colorless hadrons are in is:

$$\frac{1}{\sqrt{3}}(r\bar{r} + g\bar{g} + b\bar{b}). \tag{1.6}$$

The remaining gauge bosons mediate the electroweak force. Before electroweak sym-
metry breaking, the generators of SU(2)xU(1) correspond to the gauge fields $B, W^1, W^2, W^3,$

whose excitations are massless gauge bosons. After symmetry breaking via the Higgs mechanism, three of the bosons acquire mass and the electroweak gauge bosons are reparametrized as:

$$W^{\pm} = \frac{1}{\sqrt{2}}(W^1 \pm iW^2)Z = \cos\theta_w W^3 - \sin\theta_w B\gamma = \sin\theta_w W^3 + \cos\theta_w B \qquad (1.7)$$

where θ_w is the weak mixing angle, the massive $W^{\pm}$ and Z bosons mediate the weak force, and the massless γ is the photon which mediates EM. $W^{\pm}$ have electric charge $\pm 1e$ while the Z and γ are neutral. The isospin of $W^{\pm}$ is ± 1 and 0 for Z and γ, giving hypercharges of 0 for $W^{\pm}$ and 0 for Z and γ.

The final particle of the SM is the scalar H. H is electrically neutral and constructed to be an SU(2) doublet before electroweak symmetry breaking, with one component having weak isospin 1/2 (hypercharge -1), and the neutral component having isospin -1/2 (hypercharge 1), which includes the physical h. After electroweak symmetry breaking, three of the H components are absorbed by the gauge bosons, and the remaining physical h remains neutral. The parity of h is 1. Although H couples to all massive fermions and bosons, the decay channels that are relevant for collider searches are: $ZZ* \rightarrow 4l, WW* \rightarrow 2l2\nu, \gamma\gamma, \tau\bar{\tau}$, and $b\bar{b}$. After a decades long search, the discovery and verification of quantum numbers of H was announced by the CMS and ATLAS exeriments in 2012 [?, ?]. The four-lepton invariant mass distribution, showing the H peak at its observed mass of $m_H = 126$ GeV is shown in Figure 1.1.

1.2 Dark matter

1.2.1 Background

This section gives an overview of the most compeling sources of observational evidence for the existance of DM, the potential particles candidates for DM, and the potential methods for detecting them.

1.2.1.1 Observational evidence

The earliest indication that there may be matter in the universe that cannot be detected by conventional optical observations, so called dark matter (DM), came from measurements
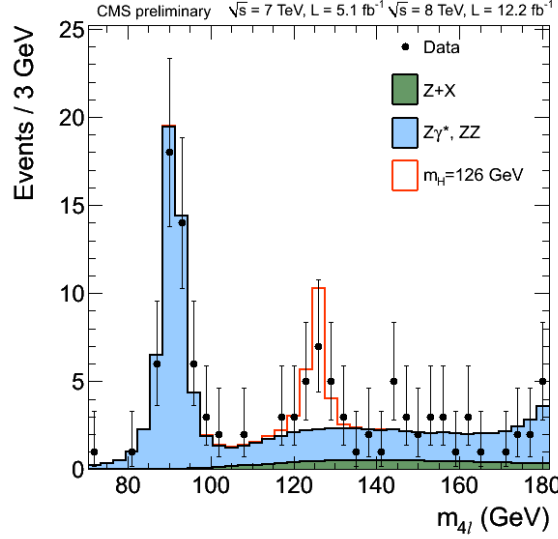
Figure 1.1: 4l invariant mass distribution showing H discovery in the ZZ* decay channel. The red line shows the signal distribution for $m_H = 126$ GeV. Figure taken from https://twiki.cern.ch/twiki/bin/view/CMSPublic/Hig12041TWiki

of the orbital velocities of astronomical bodies in galaxy clusters [?, ?] and galaxies [?, ?]. Classical Newtonian gravity gives a galactic rotation curve, which shows how the velocity v of a massive object depends on its distance r from the center of a galaxy, as $v(r) \propto \sqrt{M(r)/r}$, where $M(r)$ is the total mass in the galaxy within a radius r. However, measurements of the orbital velocities of objects outside of the visible part of galaxies, where $v(r) \propto 1/\sqrt{r}$, show instead $v(r) \propto$ const., i.e. that the mass $M(r) \propto r$ instead of being constant [?]. The larger than expected velocities imply the existance of this spherically symmetric, dark halo of non-luminous matter in galaxies.

A compelling example showing direct evidence for DM is galaxy cluster 1E0657-558, often referred to as the "bullet cluster" from its bullet-like shape [?]. The bullet cluster passed through another galaxy cluster at some point in the recent cosmological past. The luminous matter, observed by traditional optical telecopes, is seen to lag behind the total mass of the clusters, observed by studying the weak gravitational lensing of objects in the background of the two clusters. The luminous matter in each cluster lags due to its interacting electromagnetically with the luminous matter in the opposing cluster, while what is inferred to be the DM continues on a balistic trajectory, not experiencing lag due

to EM interactions [**?**].

Many other cosmological observations and theories, including observations from strong gravitational lensing in elliptical galaxies [**?**], weak lensing of distant galaxies by foreground matter [**?**], modelling of anisotropies in the cosmic microwave background (CMB) [**?**, **?**], strongly support the existence of DM, and other than a handful of competing theories which modify the laws of gravity instead of adding new matter, the existence of DM is widely accepted [**?**], and accounts for 20-40% of the mass density of the universe [**?**].

1.2.1.2   Particle candidates

From a variety of searches for different types of new dark particles, much more is known about what DM isn't than what it is. From surveys to detect gravitational microlensing from massive compact halo objects (MACHOs), such as black holes, dwarf, and neutron stars, that could be baryonic matter faking DM, these objects cannot account for the majority of DM [**?**, **?**]. In fact, Big Bang nucleosynthesis, the theory of how light nuclei were produced in the early universe, shows that measurements of the abundences of elements today suggest that most of DM is non-baryonic [**?**]. Measurements of CMB anisotropies determine the density of non-baryonic matter, an important constraint on potential DM candidates [**?**]. For example, the only SM particles that could potentially account for DM are neutrinos, but these are excluded because they are not abundent enough to account for the DM density [**?**].

For all that is unknown about the particle content of the dark sector, there are several properties of DM that are known with high confidence: it does not interact via the EM force, or this interaction is highly suppressed, it is stable over long time scales, it has a relic density consistent with cosmological observations, and it is "cold", meaning it was non-relativistic by the time galaxies were beginning to form [**?**]. A plethora of candidates satisfying these properties has been developed, including sterile neutrinos [**?**], like SM neutrinos but that do not interact via the weak force, axions [**?**], theoretical particles developed to address CP violation, and particles from "little Higgs" models [**?**, **?**], just to name a few.

The most widely studied candidates, however, are weakly interacting massive particles

(WIMPs), with masses in the 10 GeV to a few TeV range, and whose self-annihilation cross section is similar in scale to the weak strength [?]. The two best motivated WIMPs are the lightest superparticle (LSP) of supersymmetric (SUSY) models [?] and the lightest Kaluza-Klein particle (LKP) of models with extra dimensions [?]. The SUSY model should obey R-parity to gaurantee the stability of the LSP, the LSP should be neutral to satisfy constraints from searches for exotic isotopes, and is unlikely to be an ordinary sneutrino, which would have been observed in previos WIMP searches [?]. This leaves the lightest neutralino, a mixture of the gauge boson superpartner gauginos, as the best DM candidate from SUSY models. Models introducing extra spatial dimensions, such as those of Arkani-Hamed, Dimopoulos, and Dvali (ADD) [?] and Randall and Sundrum (RS)[?], predict a "tower" of excited states of SM particles, called Kaluza-Klein (KK) states, with increasing mass proportional to the inverse of the scale of the extra dimension, and having the same quantum numbers as their corresponding SM particles. Models where all SM fields can propagate in the extra dimensions, as opposed to models where only gravity can, are called universal extra dimensions (UED) [?]. The best motivated LKP is the first KK excitation in UED of the SM U(1) gauge boson [?].

1.2.1.3   Potential detection methods

The methods of detecting DM fall into three categories: indirect searches, where the products of DM annihilations or decays are observed, direct searches, where the recoil of SM particles is measured after scattering with an incident DM particle, and collider searches, where the DM candidate is produced directly from interactions of SM particles. These methods compliment one another since they approach the problem in a different way and have different relative strengths and weaknesses. For example, direct searches are limited in their sensitivities at low DM masses by the inability to measure such smaller nuclear recoils, while colliders excel in this region since the production of low mass particles is uninhibited by kinematic restrictions. Conversely, collider searches are less sensitive than direct and indirect searches at high mass, being limited by the energy scale of the collisions.

Indirect DM searches are performed at experiments designed to detect the SM prod-

ucts of the decays or self-annihilations of DM particles. Since DM is attracted by the gravitational force, it could collect in the centers of massive bodies such as the Sun or Earth, where they would be more likely to annihlate in higher densities. The IceCube detector sets the best upper limits on the high energy muon flux from DM annihilations within the Sun to 103 muons/km^2/yr [?], while the SuperKamiokande telescope has the best upper limits for softer muons at about 1500 muons/km^2/yr [?]. Searches for photons from DM annihilating in the galactic halo can produce mono-energetic photon spectra, but these signals are particularly difficult to isolate from photons of regular astrophysical origin. The FERMI/LAT collaboration has found a small signal in a region around the galactic center where known point sources were removed from the data, but the result is not strong enough to warrant a discovery [?]. Finally, DM can produce an excess in the spectra of antiparticles such as positrons. Experiments find small excesses with these signatures, but they may be explained by astrophysical sources, and predict a DM cross section too high to be consistent with a thermal WIMP [?].

Direct DM searches measure the interaction of DM with regular matter through either elastic or inelastic collisions, in either a spin-dependent or spin-independent manner in terrestrial laboratory detectors [?]. In an elastic scattering experiment, WIMPs interact with the nuclei in the detector as a whole, and the recoil energy spectrum is measured, typically in the range 1-100 keV. In inelastic scattering experiments, the WIMP either excites or ionizes orbital electrons, or the WIMP leaves the nuclei in the detector in an excited state, yielding an energy recoil of the nucleus plus an emitted photon a short time later. These target interactions are also distinguished by whether the DM-nucleon interactions involve the spin degree of freedom of the nuclei. Spin-independent detectors benefit from an increase in the DM-nucleon interaction cross section by increasing the mass of the detector nuclei, while the mass of the detector material does not benefit the spin-dependent measurements as much. The best cross section lower limits for spin-indenpendent and spin-dependent neutron interactions come from the Large Underground Xenon (LUX) detector, a time-projection chamber filled with 368 kg of scintillating liquid xenon, surrounded by highly sensitive light detectors to search for the signature of DM

scattering with a xenon atom, and shielded by a large water tank and a mile of Earth overburden [**?**]. For a WIMP mass of 33 GeV, the cross section lower limits from LUX are on the order of 10^{-45}cm^2 for spin-independent, and $10^{-41}(10^{-39})$cm^2 for spin-independent neutron(proton) interactions.

Finally, DM can be produced directly in particle colliders, and searches looking for signatures of high missing energy from the DM escaping the detector opposite a tagged SM particle can be explored. Such signatures are refered to as mono-X, where X is the single SM particles observed in the detector. It should be noted that collider searches are not DM searches in the traditional sense, where the target signal originates from the cosmic dark matter discussed above, since the DM particles are produced and not from cosmic origins. A DM-like particle produced and detected at a collider experiment, displaying some of the desired properties, may mimic the cosmic DM, but may not be stable on cosmological time scales, for example [**?**]. Since the subject of this dissertation is a collider search, this topic is covered in detail in the next section, including the current status of these searches using the ATLAS and CMS detectors at the LHC collider.

When the observations of either of the three detection methods are consistent with the backgrounds only and no signal is observed, the results are cast in the form of exclusion limits, and special care must be taken to compare these limits between the different methods. Of particular interest is the comparison of DM cross section upper limits between direct and collider searches. In order to compare the DM-nucleon cross sections from direct and indirect searches to the mono-X production cross sections from collider searches, a model for how DM couples to the nucleons must be specified. For comparisons to the spin-independent cross section upper limits for DM scattering off a nucleus N found by LUX, the following relation will be used:

$$\sigma_{\chi N}^{SI} = \frac{\mu_{\chi N}^2}{\pi}[Zf_p + (A-Z)f_n]^2 \tag{1.8}$$

where $\mu_{\chi N} =$ is the $\chi - N$ reduced mass, A and Z are the atomic mass numbers of N, and $f_{p/n}$ are the model-dependent couplings of DM to protons/neutrons [**?**]. A set of models describing the explicit coupling of DM to SM particles are detailed in the next section.

1.3 Beyond the Standard Model

1.3.1 Collider searches for DM

Previous DM searches at the Large Hadron Collider (LHC), descibed in detail in the next chapter, using the CMS (next chapter) and ATLAS detectors, include analyses with mono-X signatures: X produced in association with large missing transverse momentum (MET) from the DM escaping the detector, where X is a jet [?, ?], t/b quark [?, ?, ?], photon [?, ?, ?], lepton [?, ?], or W/Z boson [?, ?, ?]. The discovery of the Higgs boson, described in the previous chapter, has opened a new portal to searching for DM at the LHC through the mono-H signature [?, ?].

Mono-H is purely a discovery mode for DM, being unable to contribute to the combination of other mono-X analyses due to the distinct production topologies and suppressed couplings. In contrast with other mono-X signatures, in which X is emitted as initial state radiation (ISR)(see Figure 1.2a), ISR of a H is highly suppressed due to the small H-quark coupling. Therefore, the H is radiated preferentially from the new physics vertex (see Figure 1.2b), directly probing the effective DM-SM coupling. The models describing the effective vertex for the case where X comes from ISR, from now on called ISR models, couple DM to quarks either through effective field theory (EFT) operators, or explicitly with a scalar or vector mediator [?]. Since the effective vertex does not explicitly involve X, the different mono-X searches can be combined, each carrying a weight proportional to the quark-X coupling. Since the quark-H coupling is small compared to the other quark-X couplings, mono-H cannot make a strong contribution to the combination, and is therefore not included. The models that have X emitted directly from the effective vertex, from now on called discovery models, do have a well-motivated mono-H signature. These models couple DM to X directly with EFT operators or a new mediator particle, so not all mono-X analyses are combined as in the ISR case. Each mono-X signature has discovery models that motivate an enhanced DM-X coupling, so although some signatures can be combined for these models, with comperable contributions, they are usually studied independently for the different signatures. These models are called discovery models because they each allow for the detection of DM for each mono-X signature, independent

of the others. Therefore, even though the signatures contribute different amounts to the ISR model combinations, it is of critically important to look at each signature's discovery models. This dissertation will consist of the study of the discovery models for mono-H, a few of which are detailed in the next section.
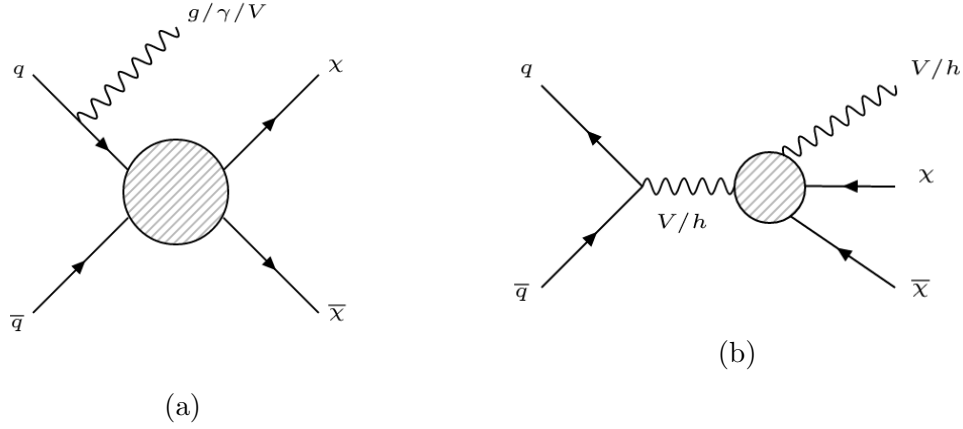

Figure 1.2: (a) Mono-X production topology for signatures with X emitted as ISR. (b) Mono-X production topology for signatures with X emitted from new physics vertex.

Mono-H searches have been done at the 8 TeV LHC for H decaying to two photons [**?**] and two b quarks [**?**] at ATLAS, with results consistent with SM predictions and limits set on various model parameters. The bb final state shows a higher sensitivity to limit setting for the models used in the data interpretation at 8 TeV. For 13 TeV LHC data, mono-H searches are being done at ATLAS for H to bb [**?**] and at CMS for the five H decay modes: ZZ, WW [**?**], $\gamma\gamma$ [**?**], bb [**?**], and $\tau\tau$ [**?**]. Each final state will have various benefits and drawbacks, with a distinct analysis dedicated to each, exploring the sensitivity to different models in different regions of parameter space.

The H→ZZ decay mode is studied in this dissertation, where the two Z bosons decay to four leptons. The mode where the Z bosons decay to two leptons and two neutrinos is open for investigation. The four lepton final state has the advantage over other H decay modes of easily reducible backgrounds and a clean reconstruction of final state particles. The three lepton combinations of four electrons, four muons, and two electrons two muons are treated individually, then combined in the final results. This channel was key to the discovery of H [**?**, **?**] at 7 and 8 TeV, and this analysis is an extension of these studies and

their continuation [**?**, **?**]. In particular, the baseline event selection used here and detailed below is chosen to match that of the other H→ZZ analysis groups through an event by event synchronization exercise [**?**].

Nine kinematically distinct models with DM are used in the data interpretation, including five effective field theory (EFT) models and four simplified models. The EFT models couple DM to H via an n-dimensional contact operator, with operators of dimension four, five, six, and eight [**?**]. They have the benefit of being independent of the details of new physics models and having a one-dimensional parameter space. The EFTs have the drawback of limited ranges of validity, being constrained by perturbativity and H and Z to invisible decay limits. The EFT parameter choices are discussed in the next section. The simplified models introduce an additional massive particle to mediate the DM-SM coupling. This mediator particle is a vector, scalar, or pseudoscalar [**?**, **?**]. Although they are better motivated by the addition of new physics, the simplified models have the drawback of more complex parameter spaces, including parameters which affect the kinematics of the final state particles and must be scanned over. The simplified model parameter choices are discussed in the next section, and are chosen to be consistent with other LHC DM searches [**?**].

1.3.2   Signal Models

The signal models are divided into two categories: effective field theories (EFTs) and simplified models.

1.3.2.1   Effective Field Theory Models and Benchmarks

The five EFTs are summarized in Table 1.2. The models have Lagrangians with effective operators ranging from dimension four to eight with either scalar or fermionic DM [**?**, **?**], producing mono-H signatures shown in Figure 1.3. The models have two parameters each, the DM mass and the coupling or mass cutoff scale. In general, the kinematics depend on the choice of both parameters, although there are regions of parameter space where the kinematics are independent of the coupling or mass cutoff scale. The DM mass values are the same for all models,

$$1, 10, 50, 65, 100, 200, 400, 800, 1000, 1300 \text{ GeV}$$

as recommended by the DMWG in [**?**]. These mass values are chosen with a fine enough grid spacing to cover the range of variation in kinematics. The additional value of 65 GeV, around half the Higgs mass, is added where the cross sections begin to drop significantly and assists in producing smooth limit curves.
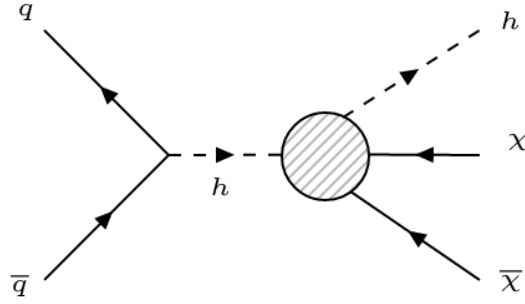

Figure 1.3: Collider production diagram for mono-H EFTs.

The value of the coupling must be set for each model individually so as to ensure the value is in a range where the kinematics are independent of the coupling. In these regions of parameter space, cross section limits can be reliably scaled to coupling limits. The additional value of $\Lambda = 1000 GeV$ for EFT_xdxHDHc is included to compare with Run 1 limits even though it is in the region where the kinematics depend on the coupling. Existing constraints on the couplings from perturbativity [**?**] and invisible branching ratio limits [**?**, **?**] are shown in Table 1.3. The constraints from invisible branching ratio limits only apply when the DM mass is less than half the mediator mass, allowing this decay to be kinematically open. The production cross sections for these benchmark choices are given in Appendix A.

1.3.2.2   Simplified Models

There are four simplified models, each including one or more new massive particles that mediate the H-DM interaction. The models with vector mediators are motivated by the addition of new symmetries to the Standard Model, with the mediator corresponding to the gauge boson of the new symmetry. Additional models are motivated by the addition of scalar or pseudoscalar mediators as a portal into the dark sector.

Name	Operator	Param.	Dim.	S_χ
EFT_HHxx_scalar	$\lambda|H|^2\chi^2$	$m_\chi, \lambda = 0.1$	4	0
EFT_HHxx_combined	$\frac{1}{\Lambda}|H|^2\bar{\chi}\chi$	$m_\chi, \Lambda = 1000$ GeV	5	1/2
EFT_HHxxg5x	$\frac{1}{\Lambda}|H|^2\bar{\chi}i\gamma_5\chi$	$m_\chi, \Lambda = 100$ GeV	5	1/2
EFT_xdxHDHc	$\frac{1}{\Lambda^2}\chi^\dagger i\partial^\mu\chi H^\dagger iD_\mu H$	$m_\chi, \Lambda = 100, 1000$ GeV	6	0
EFT_xgxFHDH	$\frac{1}{\Lambda^4}\bar{\chi}\gamma^\mu\chi B_{\mu\nu}H^\dagger D^\nu H$	$m_\chi, \Lambda = 200$ GeV	8	1/2

Table 1.2: Effective Field Theory Models.

Name	Perturbativity	BR_{inv} Limits
EFT_HHxx_scalar	$\lambda < 4\pi$	$\lambda < 0.016$ $(m_\chi < m_h/2)$
EFT_HHxx_combined	$\Lambda > v/4\pi$	$\Lambda > 10$ TeV $(m_\chi < m_h/2)$
EFT_HHxxg5x	$\Lambda > v/4\pi$	$\Lambda > 10$ TeV $(m_\chi < m_h/2)$
EFT_xdxHDHc	$g_Z < 4\pi, \Lambda > 30$ GeV	$\Lambda > 400$ GeV $(m_\chi < m_Z/2)$

Table 1.3: Constraints on EFT parameters.

1.3.2.3   Z' - Two Higgs Doublet Model

The Z' - Two Higgs Doublet Model (Zp2HDM) simplified model extends the gauge group of the SM in include a new symmetry, $U(1)_{Z'}$, with Z' the gauge boson [?]. This symmetry is spontaneously broken by a scalar singlet ϕ, generating a Z' mass above the EW symmetry breaking scale. The right-handed quarks are charged under $U(1)_{Z'}$ and all other SM particles are neutral. The Z' coupling to quarks, g_z, is constrained by EW global fits [?] and dijet resonance searches [?, ?] to be

$$g_z < 0.03\frac{g}{\cos\theta_w\sin^2\beta}\frac{\sqrt{M_{Z'}^2 - M_Z^2}}{M_Z}. \tag{1.9}$$

Additionally, a second Higgs doublet is added with a Type 2 two-Higgs doublet model, introducing states Φ_u and Φ_d, which couple to up and down type quarks respectively as

$$\mathcal{L} \supset -y_u Q\bar{\Phi}_u\bar{u} - y_d Q\Phi_d\bar{d} + y_e L\Phi_d\bar{e} + h.c.. \tag{1.10}$$

Φ_u is chosen to be charged under $U(1)_{Z'}$, while Φ_d is neutral. The two Higgs doublets obtain vevs ν_u and ν_d after EW symmetry breaking and can be parametrized as

$$\Phi_d = \frac{1}{\sqrt{2}}\left(-\right)\sin(\beta)H^+\nu_d-\sin(\alpha)h+\cos(\alpha)H-i\sin(\beta)A^0 \quad \Phi_u = \frac{1}{\sqrt{2}}\left(\cos\right)(\beta)H^+\nu_u+\cos(\alpha)h+\sin(\alpha)H+i$$

(1.11)

where h and H are neutral CP-even scalars and A^0 is CP-odd. The angle α is defined as the angle that diagonalizes the $h - H$ mass mixing matrix, and the angle β is defined as $\tan(\beta) = \nu_u/\nu_d$. h is assumed to be the SM Higgs boson with $m_h = 125$ GeV, while the other scalars have masses > 300 GeV. Due to perturbativity and previous constraints [?], α and β are chosen such that $\tan(\beta) > 0.3$ and $\alpha = \beta - \pi/2$.

Mono-Higgs signals arise when the pseudoscalar A^0 has a large branching ratio to DM, as shown in Figure 1.4. The new particles and parameters of the Zp2HDM model are summarized in Table 1.4. The values of the parameters chosen for various benchmark scenarios are given in the next section.
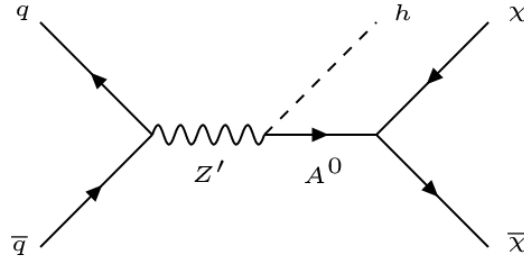
Figure 1.4: Collider production diagram for Zp2HDM.

1.3.2.4   Baryonic Z' Model

The Baryonic Z' (ZpBaryonic) simplified model extends the gauge group of the SM to include a new symmetry, $U(1)_B$ for the baryon number B, with the Z' being the gauge boson of $U(1)_B$ [?, ?, ?]. Z' couples to quarks and fermionic DM as

$$\mathcal{L} \supset g_q\bar{q}\gamma^\mu q Z'_\mu + g_\chi\bar{\chi}\gamma^\mu\chi Z'_\mu$$

(1.12)

To derive a mono-Higgs signature, $U(1)_B$ is spontaneously broken by a "baryonic

Particle	Description
χ	Fermionic DM particle
Z'	$U(1)_{Z'}$ gauge boson
ϕ	Z' sector scalar
Φ_u, Φ_d	Two Higgs doublets
h, H	Neutral CP-even scalars
$H^\pm$	Charged heavy Higgs
A^0	Neutral CP-odd pseudoscalar
Param.	Description
m_χ	DM mass
$m_{Z'}$	Z' mass
g_z	Z'-quark coupling
$y_{u/d/e}$	Φ-up-quark/down-quark/lepton coupling
$\nu_{u/d}$	$\Phi_{u/d}$ vev
α	h-H mixing angle
β	$\Phi_{u/d}$ vev angle

Table 1.4: Zp2HDM simplified model

Higgs" scalar h_B, which mixes with the SM Higgs via a mixing angle θ. This mixing induces an h-Z' interaction $-g_{hZ'Z'}hZ'_\mu Z'^\mu$ with coupling

$$g_{hZ'Z'} = \frac{m_{Z'}^2 \sin(\theta)}{\nu_B} \tag{1.13}$$

where $m_{Z'}$ is the mass of the Z' and ν_B is the vacuum expectation value (vev) of h_B. At energies less than $m_{Z'}$, these operators combine to yield an effective Lagrangian

$$\mathcal{L}_{eff} = -\frac{g_q g_\chi}{m_{Z'}^2}\bar{q}\gamma^\mu q \bar{\chi}\gamma_\mu\chi(1 + \frac{g_{hZ'Z'}}{m_{Z'}^2}h) \tag{1.14}$$

The first term gives rise to mono-jet and mono-EW boson signals, while the second yields the mono-Higgs signal shown in Figure 1.5.
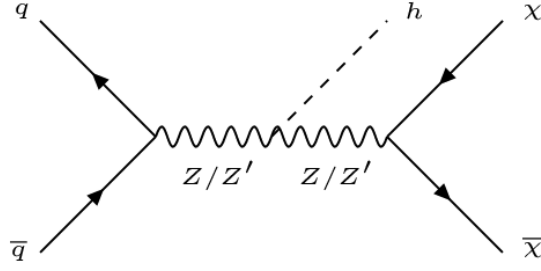
Figure 1.5: Collider production diagram for Z' models.

The new particles and parameters of the ZpBaryonic model are summarized in Table 1.5. Perturbativity arguments require the Z'-quark coupling to be less than 4π [?]. The values of the parameters chosen for various benchmark scenarios are given in the next section.

Particle	Description
χ	Fermionic DM particle
Z'	$U(1)_B$ gauge boson
h_B	Baryonic Higgs
Param.	Description
m_χ	DM mass
$m_{Z'}$	Z' mass
g_q	Z'-quark coupling
g_χ	Z'-DM coupling
$g_{hZ'Z'}$	Z'-h coupling
θ	h-h_B mixing angle
ν_B	h_B vev

Table 1.5: ZpBaryonic simplified model

1.3.2.5   Hidden Sector Z' Model

The Hidden Sector Z' (ZpHS) simplified model mixes the SM and a hidden sector with a $U(1)'$ symmetry [?, ?, ?, ?, ?]. SM particles are neutral under $U(1)'$ while DM is charged.

The relevant terms in the Lagrangian are

$$\mathcal{L}_{eff} \supset \frac{g_2}{2c_W} J^\mu_{NC} Z_\mu + g_\chi \bar\chi \gamma^\mu \chi Z'_\mu \qquad (1.15)$$

where J_{NC} is the SM neutral current. A mono-Higgs signature arises from a $Z - Z'$ mass mixing, which is diagonalized by the rotation

$$Z \rightarrow \cos(\theta)Z - \sin(\theta)Z', Z' \rightarrow \cos(\theta)Z' + \sin(\theta)Z \qquad (1.16)$$

This mixing yields the mono-Higgs signatures shown in Figure 1.5 through the $h - Z - Z'$ interaction

$$\mathcal{L}_{eff} \supset \frac{m_Z^2 \sin(\theta)}{\nu} h Z'_\mu Z^\mu \qquad (1.17)$$

The new particles and parameters of the ZpHS model are summarized in Table 1.6. In order to be consistent with the invisible Z width of $\Lambda(Z \rightarrow \chi\bar\chi) < 3$ MeV, the value of θ is constrained by $\sin\theta < 0.03$ for $m_\chi < m_z/2$ [?]. The values of the parameters chosen for various benchmark scenarios are given in the next section.

Particle	Description
χ	Fermionic DM particle
Z'	$U(1)'$ gauge boson
Param.	Description
m_χ	DM mass
$m_{Z'}$	Z' mass
g_χ	Z'-DM coupling
θ	Z-Z' mixing angle

Table 1.6: ZpHS simplified model

1.3.2.6   Scalar Mediator Model

The Scalar Mediator (Scalar) simplified model introduces a real scalar singlet S as a portal into the dark sector [?]. The quark and DM Yukawa coupling terms are

$$\mathcal{L} \supset -y_\chi \bar{\chi}\chi S - \frac{m_q}{\nu}\bar{q}qh \qquad (1.18)$$

and the relevant terms of the scalar potential are

$$V \supset a|H|^2 + b|H|^2 S^2 + \lambda_h |H|^4 \rightarrow \frac{1}{2}a(h+\nu)^2 S + \frac{1}{2}b(h+\nu)^2 S^2 + \frac{\lambda_h}{4}(h+\nu)^4. \quad (1.19)$$

The expression after the arrow follows when the Higgs acquires a vev, as $H \rightarrow \frac{1}{\sqrt{2}}(h+\nu)$. After expanding the expression, there is an h-S mixing term $a\nu hS$. The system can be diagonalized with the rotation

$$h \rightarrow \cos(\theta)h + \sin(\theta)S, S \rightarrow \cos(\theta)S - \sin(\theta)h \qquad (1.20)$$

where θ is defined by $\sin(2\theta) = 2a\nu/(m_S^2 - m_h^2)$. Following this rotation, the Yukawa terms become

$$\mathcal{L} \supset -y_\chi \bar{\chi}\chi(\cos(\theta)S - \sin(\theta)h) - \frac{m_q}{\nu}\bar{q}q(\cos(\theta)h + \sin(\theta)S) \qquad (1.21)$$

and the relevant terms in the scalar potential, at first order in $\sin(\theta)$, are

$$V \supset \frac{\sin(\theta)}{\nu}(2m_h^2 + m_S^2)h^2 S + b\nu hS^2. \qquad (1.22)$$

These terms give rise to the mono-Higgs interactions shown in Figure 1.6, as well as additional loop diagrams for gluon fusion production. The new particles and parameters of the Scalar model are summarized in Table 1.7. Perturbativity arguments require $\sin\theta < 4\pi$ [?] while 8 TeV Higgs data is consistent with $\cos\theta = 1$, requiring $\sin\theta < 0.4$ [?, ?, ?, ?]. The values of the parameters chosen for various benchmark scenarios are given in the next section.

1.3.2.7   Benchmarks

The simplified models are summarized in Table 1.8. Although these models have better physical motivations, the parameter spaces are vastly more complex than the EFTs, making it difficult to understand the cross section scaling rules and kinematic dependence
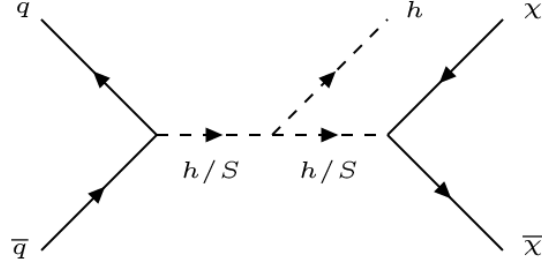
Figure 1.6: Collider production diagram for Scalar model.

Particle	Description
χ	Fermionic DM particle
S	Scalar particle
Param.	Description
m_χ	DM mass
m_S	S mass
y_χ	S-DM coupling
a, b	h-S scalar couplings
θ	h-S mixing angle

Table 1.7: Scalar simplified model

on parameters accross the entire parameter spaces. The parameter values are chosen to match the recommendations of the DMWG []. For the ZpHS (Z' Hidden Sector) model, which is not included in the DMWG report, the coupling parameters are chosen to match the benchmarks in Ref[] while the DM and mediator mass scan matches the DMWG recommendations for a vector mediator, shown in Table 1.10. The DM and mediator mass scans for the Zp2HDM and Scalar models are shown in Table 1.11 and Table 1.12, respectively. Existing constraints on the couplings from theory and invisible branching ratio limits given in Ref[] are shown in Table 1.9. The production cross sections for the simplified models are given in Appendix A.

Name	Mediator(S_{Mediator})	Fixed Param.	Scanned Param.
Zp2HDM	Z'(1/2), $A^0(0)$	$m_\chi = 100$ GeV, $g_Z = 0.8$, $\tan\beta = 1$	$(m_{Z'}, m_{A^0})$ = Table 1.11
ZpBaryonic	Z'(1/2)	$g_\chi = 1$, $g_q = 1/3$, $g_{hZ'Z'} = m_{Z'}$	$(m_{Z'}, m_\chi)$ = Table 1.10
ZpHS	Z'(1/2)	$g_\chi = 1$, $\sin(\theta) = 0.1$	$(m_{Z'}, m_\chi)$ = Table 1.10
Scalar	S(0)	$g_\chi = 1$, $\sin(\theta) = 0.3$, $b = 3$	(m_S, m_χ) = Table 1.12

Table 1.8: Simplified Models.

Name	Perturbativity	BR_{inv} Limits
Zp2HDM		
ZpBaryonic	$g_q < 4\pi$	N/A
ZpHS	N/A	$\sin(\theta) < 0.03$ ($m_\chi < m_Z/2$) [21]
Scalar	$\sin 2\theta < 4\pi$	$\sin\theta < 0.4$ [6,38-41]

Table 1.9: Constraints on simplified model parameters.

m_χ [GeV]	$m_{Z'}$ [GeV]									
1	10	20	50	100	200	300	500	1000	2000	10000
10	10	15	50	100						10000
50	10		50	95	200	300				10000
150	10				200	295	500	1000		10000
500	10						500	995	2000	10000
1000	10							1000	1995	10000

Table 1.10: Mass points for models with a vector mediator.

1.4   Production Cross Sections for Benchmark Signal Models

m_{A^0} [GeV]	$m_{Z'}$ [GeV]							
300	600	800	1000	1200	1400	1700	2000	2500
400	600	800	1000	1200	1400	1700	2000	2500
500		800	1000	1200	1400	1700	2000	2500
600		800	1000	1200	1400	1700	2000	2500
700			1000	1200	1400	1700	2000	2500
800			1000	1200	1400	1700	2000	2500

Table 1.11: Mass points for Zp2HDM.

m_χ [GeV]	$m_{Z'}$ [GeV]								
1	10	20	50	100	200	300	500	1000	10000
10	10	15	50	100					10000
50	10		50	95	200	300			10000
150	10				200	295	500	1000	10000
500	10						500	995	10000
1000	10							1000	10000

Table 1.12: Mass points for models with a scalar mediator.

m_χ [GeV]	1	10	50	65	100	200	400	8
EFT_HHxx_scalar	0.10071E+01	0.99793E+00	0.60671E+00	0.48291E-04	0.22725E-05	0.11059E-06	0.36569E-08	0.407
EFT_HHxx_combined	0.15731E+01	0.15194E+01	0.34134E+00	0.41039E-04	0.10581E-04	0.16553E-05	0.14628E-06	0.406
EFT_HHxg5x	0.15735E+03	0.15594E+03	0.94804E+02	0.12990E-01	0.23075E-02	0.41820E-03	0.45743E-04	0.167
EFT_xdxHDHc								
$\Lambda = 100$ GeV	0.29530E+00	0.29067E+00	0.10540E+00	0.89849E-01	0.64959E-01	0.30639E-01	0.88644E-02	0.979
$\Lambda = 1000$ GeV	0.16306E-04	0.15508E-04	0.12088E-05	0.88288E-06	0.53312E-06	0.18046E-06	0.34918E-07	0.275
EFT_xgxFHDH	0.57027E+00	0.57001E+00	0.56025E+00	0.55337E+00	0.53270E+00	0.45792E+00	0.29777E+00	0.1028

Table 1.13: EFT model production cross sections [pb]

m_χ [GeV]	m_S [GeV]								
1	0.21915E+01	0.20798E+01	0.19192E+01	0.18118E+01	0.16735E+01	0.52244E+01	0.41877E+01	0.28732E+01	0.1
10	0.17416E+01	0.17420E+01	0.18581E+01	0.17510E+01		0.12861E+01			0.1
50	0.39053E+00		0.38877E+00	0.38409E+00	0.37097E+00				0.3
150	0.24136E-05				0.38372E-05	0.21922E-04	0.42337E-03	0.57124E-04	0.
500	0.34099E-08						0.49399E-08	0.25206E-06	0.
1000	0.17012E-10							0.55260E-10	0.

Table 1.14: Scalar model production cross sections [pb] corresponding to mass points in Table 1.12

m_χ [GeV]	$m_{Z'}$ [GeV]							
1	0.26615E+01	0.27802E+01	0.33248E+01	0.32341E+01	0.26566E+01	0.23191E+01	0.10842E+01	0.18700E+00
10	0.21182E-01	0.74027E-01	0.32732E+01	0.32250E+01	0.21226E+01	0.20120E+01	0.67266E+00	0.18111E+00
50	0.36342E-03		0.12726E-01	0.31337E+00	0.56526E-02	0.18000E+00		0.10368E-01
150	0.55972E-05							
500	0.80295E-08						0.36591E-04	
1000	0.49387E-10							0.98079E-06

Table 1.15: ZpBaryonic model production cross sections [pb] corresponding to mass points in Table 1.10

m_χ [GeV]	$m_{Z'}$ [GeV]								
1	0.61935E-02	0.63192E-02	0.82991E-02	0.11942E-01	0.19171E-01	0.21560E-01	0.16010E-01	0.64416E-02	0.26526E-0
10	0.58781E-02	0.58938E-02	0.82944E-02	0.11937E-01					
50	0.10294E-03		0.77820E-04	0.15258E-04	0.12066E-01	0.12105E-01			
150	0.28382E-06				0.839917E-05	0.72889E-03	0.65401E-02	0.68337E-03	0.28292E-0
500	0.34689E-09						0.43355E-06	0.87799E-04	
1000	0.20703E-11							0.44782E-07	0.19974E-0

Table 1.16: ZpHS model production cross sections [pb] corresponding to mass points in Table 1.10

m_{A^0} [GeV]	$m_{Z'}$ [GeV]							
300	42.386	45.097	35.444	26.07	18.942	11.778	7.4456	3.6446
400	5.8513	14.847	14.534	11.792	9.029	5.851	3.7819	1.8758
500		5.9605	8.4961	7.9575	6.5515	4.5063	3.0028	1.5235
600		1.5853	4.6972	5.4808	4.9946	3.7044	2.5694	1.3447
700			2.1092	3.4848	3.6766	3.0253	2.2023	1.1984
800			0.65378	1.9638	2.5511	2.4077	1.8689	1.0692

Table 1.17: Zp2HDM model production cross sections [pb] corresponding to mass points in Table 1.11

Chapter 2

Experimental apparatus

This chapter gives an overview of the experimental apparatus used to collect the data analyzed in this dissertation: the Large Hadron Collider (LHC) and Compact Muon Solenoid (CMS) detector. The first section reviews the design and performance of the LHC. The second section reviews the design of CMS, its component subdetectors, and data acquisition system.

2.1   Large Hadron Collider

This section reviews the construction and original design specifications of the LHC [?], leading up to the 7-8 TeV center of mass (COM) energy collisions recorded from March 2010 to February 2013 (Run 1), the upgrades and repairs made to the LHC and its pre-accelerators during Long Shutdown 1 (LS1) from February 2013 to April 2015, and finally, the 13 TeV COM energy collisions recorded from April 2015 through 2016.

Due to budgetary and logistical concerns, the LHC is located in the repurposed Large Electron-Positron (LEP) collider tunnel, constructed in the 1980s by the European Organization for Nuclear Research (CERN), which continues to operate the LHC accelerator facilities and whose laboratory hosts the staff, scientists, and engineers running the machines and detectors associated with it. Located beneath the border of Switzerland and France near Geneva, the LEP tunnel consists of eight straight sections and eight arced sections, totalling 26.7 km, at depths varying from 45 m to 170 m. Two 2.5 km transfer tunnels connect the main LEP tunnel to the rest of the CERN complex, which includes a

series of pre-accelerators that increase the energy of ionized hydrogen gas protons to 450 GeV before they are injected into the LHC. In addition to repurposing the tunnel, the underground caverns at Points 2 and 8, which were built for LEP, are used for the ALICE and LHCb experiments, the two specific purpose experiments, designed to study quark-gluon plasma in heavy ion collisions and the matter-antimatter imbalance, respectively. The facilities at Points 1 and 5, where the general-purpose ATLAS and CMS experiments are located, were built new for the LHC.

Although the length of the LEP tunnel is sufficient for the LHC, the diameter of the tunnel and the geometry of the straight and arced sections are suboptimal for a proton-proton accelerator. Since sychrotron radiation emission is not as much of a problem for a protons, the LHC would ideally have longer arced sections. The two counter circulating particle-antiparticle beams of LEP could occupy the same pipe, being curved by the same magnets, but with an inside diameter of only 3.7 m, the tunnel is too narrow to accommodate the two pipes needed for counter circulating proton-proton beams, necessitating the use of the "two-in-one" super-conducting twin bore magnet design. The LHC beam is steered by 1232 8 T, superconducting dipole twin bore magnets, which are cooled by a system of NbTi Rutherford cables to below 2 K. This technology is essential to the LHC operation, but comes at the cost of a higher sensitivity to instabilities in the operation temperature, which may cause the magnet to quench, or lose its superconductivity and current.

The LHC was designed to explore physics at the EW symmetry breaking scale, with a nominal COM energy for collisions of 14 TeV, and search for rare events produced by physics beyond the SM, with a target luminosity of $10^{34}\text{cm}^{-2}\text{s}^{-1}$, both the highest ever produced. For a general physics process, the rate of event production is given by

$$N = \sigma \times L \propto \sigma \times n_b N_b^2 f_{rev} \gamma \tag{2.1}$$

where σ is the process cross section, L is the LHC luminosity, which is proportional to n_B, the number of bunches per beam, N_b^2, the number of particles per bunch, f_{rev}, the beam revolution frequency, and γ, the relativistic gamma factor. Consequently, to achieve higher event rates for rare processes, both high beam intensities and high beam energies are

required. To search for rare events, such as H production, the basic strategy for designing the LHC was to maximize these luminosity parameters within the budgetary, engineering, and physical limitations, of which there are many. Combining these constraints yields nominal values of 2808 bunches per beam, 1.2×10^{11} protons per bunch, and a revolution frequency of 11245 turns per second. The luminosity decays over a given run with a lifetime of $\tau \approx 15$ hours, due primarily to losses in particle intensity from collisions, and must periodically be dumped and refilled with an average turnaround time of around 7 hours. The integrated luminosity is the integral of the luminosity as a function of time $L(t) = L_0/(1 + t/\tau)^2$ over a run of length T_{run} given by

$$L_{int} = L_0 \tau (1 - e^{-T_{run}/\tau}) \tag{2.2}$$

where L_0 is the initial luminosity. If the LHC runs for 200 days per year with a peak luminosity of $10^{34} \mathrm{cm}^{-2}\mathrm{s}^{-1}$, the maximum total integrated luminosity, or sum of the integrated luminosity of all runs is about $80\mathrm{fb}^{-1}$ per year. Due to unforeseen setbacks and inefficiencies in collecting data at the detectors, the total integrated luminosity collected by the experiments is far less than the maximum, totalling around $20\mathrm{fb}^{-1}$ each from ATLAS and CMS in the whole Run 1, and about $2\mathrm{fb}^{-1}$ each in 2015.

The LHC machine was designed to attain a per beam energy of 7 TeV, resulting in COM collisions of 14 TeV, but an accident during beam energy ramp-up in September 2008, caused by a faulty electrical connection between two magnets and resulting in the damage of numerous magnets, resulted in delays [http://press.cern/press-releases/2008/10/cern-releases-analysis-lhc-incident]. As a result, the Run 1 beam energy was set to 3.5 TeV and later increased to 4 TeV, for 7 and 8 TeV collisions. LS1 began at the conclusion of Run 1, and consisted of a two year period of maintenance and upgrades, including consolidating and repairing interconnections between about 500 magnet cryostats, adding shielding and relocating various electronic equipment, and upgrades to the LHC's ramp up accelerators [http://home.cern/about/updates/2013/02/long-shutdown-1-exciting-times-ahead]. It was decided that Run 2 would proceed with beam energies of 6.5 TeV instead of the originally planned 7 TeV in the interest of time, since it would have taken longer to retrain the magnets to not quench below currents required for 14 TeV than

it would to retrain them for 13 TeV [http://home.cern/about/engineering/restarting-lhc-why-13-tev]. Overall, the LHC has performed and continues to perform at a very high level, supplying the experiments with beam collisions within the desired luminosity ranges.

2.2   Compact Muon Solenoid

This section reviews the design and performance of the CMS detector [**?**], including its general layout, subdetector systems, and trigger and data acquisition (DAQ) systems. CMS was designed to explore physics at the TeV scale, recording collisions from the LHC proton beams at their crossing place at Point 5, near Cessy, France. The detector is multi-purpose, in that it is sensitive to detecting a wide array of new physics signatures, but the primary purpose is to validate or refute the Higgs mechanism as being responsible for EW symmetry breaking. This goal was accomplished in Run 1, so Run 2 looks forward to searching for physics beyond the SM, including signatures from new symmetries such as SUSY, extra dimensions, and dark matter. Additionally, CMS is disigned to record collisions of heavy ion beams to study QCD at this energy scale. CMS is distinguished from other general purpose detectors by its high magnetic field solenoidal structure, silicon-based inner tracker, and crystal scintillator electromagnetic calorimeter.

The primary challenges in designing CMS include: accounting for the pileup of inelastic collisions on each event with sufficiently high granularity detectors and small timing resolutioin, ensuring all electronics and detector components can withstand the high radiation exposure, and triggering on the roughly 10^9 events per second to filter out interesting events to a rate managable by the read out and computing systems. The design requirements can be summarized as follows: good muon identification and charge determination, good charged-particle momentum resolution in the inner tracker, good EM energy resolution, good diphoton, dimuon, dijet, and dielectron mass resolutions, efficient photon and lepton isolation, and good MET measurement. All of these requirements will be addressed in the remainder of this chapter.

With an overall length of 21.6 m and an outer diameter of 14.6 m, the cylindrical shape of CMS is divided into two regions, the barrel and endcaps, with the coordinate

system centered at the collision point near the center of the cylinder. The standard coordinate definitions have the x-axis pointing inward toward the center of the LHC, the y-axis pointing upward, and the z-axis in the beam direction in a right-handed manner. The polar coordinates r and ϕ are measured in the x-y plane, transverse to the beam, where the transverse momentum quantity p_T is defined. The missing energy E_T^{miss} is defined as the imbalance in measured p_T. The polar angle θ is measured from the z-axis. A convenient coordinate for relativistic measurements is the pseudorapidity, defined as $\eta = -\ln\tan(\theta/2)$.
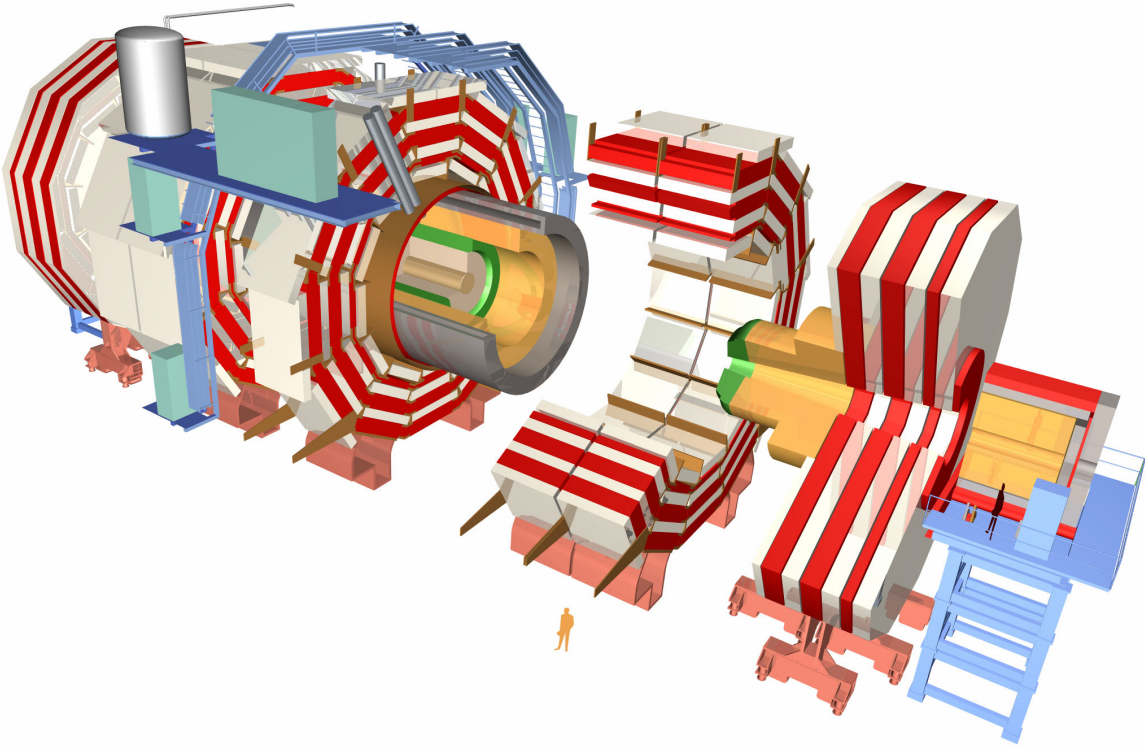

Figure 2.1: Deconstructed view of the CMS subdetectors, with human figure for scale. From inside to out, the colored segments correspond to the following systems: light brown is the pixel tracker, cream is the strip tracker, green is the ECAL, orange is the HCAL, grey is the solenoid, red is the yoke with white muon chambers.

The dominant feature of CMS is the superconducting solenoid, 13 m long and 6 m in diameter, supplying a field of 4 T required to bend charged particles at the energies produced in up to 14 TeV collisions for the momentum and charge measurements. Within and surrounding the solenoid is a series of layered detectors and support structure, a cutout

of which is shown in Figure 2.1. At the center of CMS, surrounding the beam interaction point, is the inner tracker, a combination of 10 layers of silicon microstrip detectors and 3 layers of silicon pixel detectors, which provide the required granularity for high occupancy collisions. The next layer, still within the solenoid bore, contains the calorimeters, first the electromagnetic calorimeter (ECAL), surrounded by the hadronic calorimeter (HCAL). The ECAL uses avalanche photodiodes in the barrel and vacuum photodiodes in the endcaps to read out scintillation light from lead tungstate crystals, produced by charged particle interactions. The HCAL in the barrel uses hybrid photodetectors to read scintillation light from hadronic interactions with the brass/scintillator detector material. The scintillation light is carried to the photodetectors with clear fibres, from wavelength shifting fibres embedded in the scintillator material. The various endcap HCAL systems ensure full coverage for measuring the missing energy. Finally, muon detecting stations are incorporated into and surround the solenoid support structure where the return field is present, including aluminum drift tubes (DTs) in the barrel and cathode strip chambers (CSCs) in the endcaps. The subdetector systems of CMS are covered in greater detail in the remainder of this chapter.

2.2.1   Tracking detectors

The inner tracking detectors of CMS, supported by a 5.30 m long tube with an inner diameter of 2.38 m suspended from the HCAL barrel, contain 1440 pixel and 15148 strip detector modules, composing the pixel detector and silicon strip tracker, respectively. The detectors are responsible for measuring the trajectories of charged particles, essential to measuring the momenta of particles with energy > 1 GeV in the range $|\eta| < 2.5$, and reconstructing secondary vertices and impact parameters, needed to ID heavy flavor particles. Being closest to the beam interaction point (IP), the tracking detectors are subjected to the highest radiation doses, and their material may interfere with the trajectories of primary particles through multiple scattering, bremsstrahlung, photon conversion, or nuclear interactions, necessitating the use of silicon technology. Additionally, due to the high particle flux of around 1000 particles per 25 ns bunch crossing, the detectors must have high granularity to resolve the trajectories of particles reliably, and fast readout times to

reduce occupancy from high flux and pileup conditions.

The detector modules of the tracking detector are shown schematically in Figure 2.2. The innermost section, labeled PIXEL, is the pixel detector, composed of 66 million $100 \ \mu m \times 150 \ \mu m$ pixels on modules layered in three barrels at radii 4.4, 7.3, and 10.2 cm and two disks on each end at $z = \pm 34.5, \pm 46.5$ cm. A deconstructed barrel pixel module is shown in Figure 2.3, with the sensor bump-bonded onto read out chips (ROCs) controlled and powered by high-density-interconnect (HDI) boards. When a charged particle passes through a pixel sensor, consisting of n-type pixels implanted on a high-resistance n-type substrate, charge carriers are induced in the conduction band of the substrate. These charge carriers then drift in the 4 T magnetic field to the nearby pixels (called charge sharing), where an analog signal is read out, amplified, and digitized by the ROC. The endcap pixel modules have a similar construction, but with different pixel sensor geometries, called plaquettes. The pixel detector has a resolution of 10-40 μm, sufficient for the imposed design requirements.
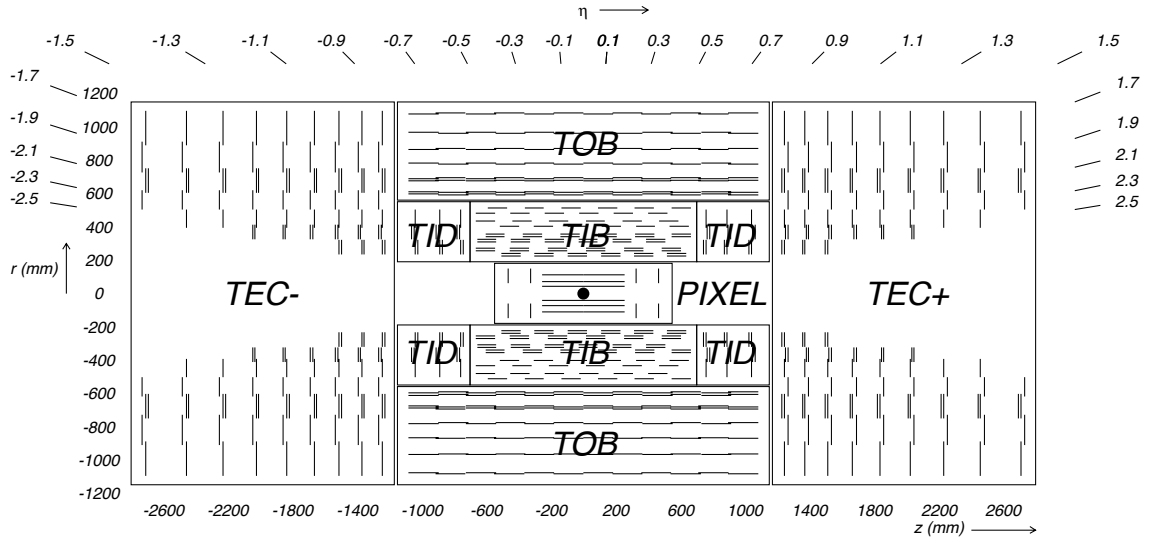

Figure 2.2: Schematic diagram of tracking detectors with radial distance of modules (shown as black lines) from center on the left axis, z-dimension on the bottom axis, and η accross the top.

The remaining modules of the tracking detector form the strip tracker, which fills the volume between 20-116 cm radially, and ± 118 cm in z. These 15,148 modules are divided into the following sections: tracker inner barrel (TIB), with four layers, tracker
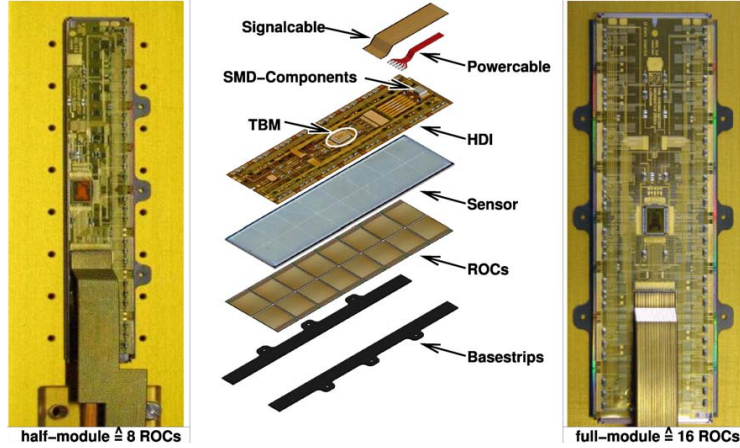
Figure 2.3: Deconstructed barrel pixel module showing module components.

outer barrel (TOB), with six layers, tracker inner disks (TID), with 6 layers, and tracker end caps (TEC), with 9 layers. The average particle occupancy at distances greater than 20 cm from the IP is low enough compared to regions closer to the beam line that the strip tracker is not required to have the same granularity as the pixel detector, thus, 29 different strip module designs, of different sizes and orientations are used. The physical principles behind the strip tracker are the same as the pixel detector; charged particles liberate conduction band electrons in the material, which drift toward read out sensors. To enhance the effect of the charge carriers drift in the magnetic field, the strip detectors are tilted, yielding a resolution around 30μm. Excluding defective modules, The detection efficienty of the strip tracker is nearly 100% (Figure 2.4) **??**.

2.2.2   Electromagnetic calorimeter

The electromagnetic calorimeter (ECAL) consists of 61200 lead tungstate crystal modules in the barrel region (EB), covering $|\eta| < 1.479$, and 7324 modules in each endcap (EE), covering $1.479 < |\eta| < 3$. The crystals are oriented radially, as shown in Figure 2.5, at angles around three degrees in the EB and two to eight degress in the EE from the vector to the IP to avoid cracks where particles would escape, arranged in various supercrystal geometries combined to form supermodules in the EB and two Dees on each endcap. The front faces of the EB crystals are at $r = 1.29$m, and present a cross section around 22×22 mm^2. The EB extends to an outer radius of 1.77 m. The endcap envelopes are
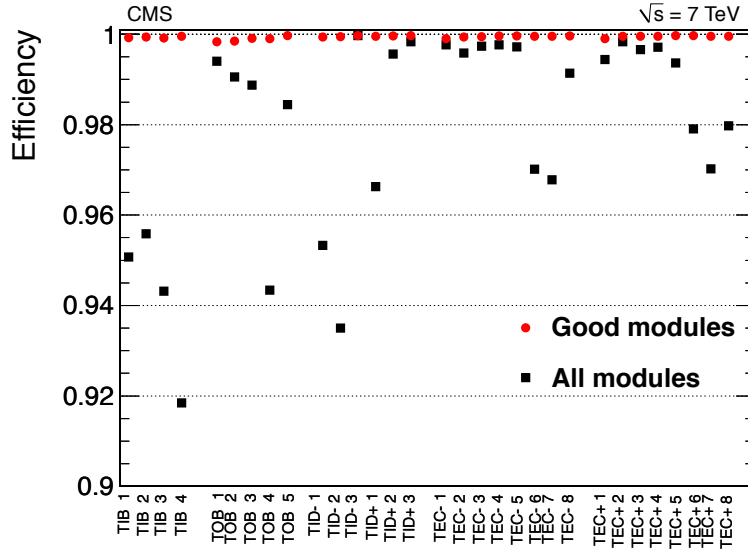
Figure 2.4: Average hit efficiencies of the strip tracker layers.

at ±315.4cm relative to the IP in z. The crystals themselves have a truncated pyramidal shape, polished on all sides to increase internal reflection, except one face on EB crystals is depolished to account for nonuniformity in light production from the crystal shape.

The ECAL is responsible for recovering the energy of electrons and photons from the showers of scintillation light they produce in the crystals. The accuracy of this measurement is of particular importance in the design of CMS since the H decay to photons and leptons are key channels in the H search, one of the primary purposes of CMS. The ECAL also contains preshower detectors in front of each set of endcap crystals, consisting of a thin layer of lead followed by a thin layer of silicon strip sensors to create and detect showers from minimum ionizing particles. The primary purpose of the preshower detectors are to identify and veto neutral pion production, in addition to improving the overall position resolution of the ECAL.

Lead tungstate crystals were chosen for the construction of the ECAL because of their hardness to the high radiation exposure, and the following properties which enable a compact detector with sufficiently high granularity: a high density of 8.28 g/cm^3, a short radiation length of 0.89 cm, and a small Moliere radius of 2.2 cm. Additionally, the crystals have a fast scintillation decay time of about 25 ns, the same time between bunch crossings, enabling fast response and read out. At operating temperature, about 4.5 photoelectrons
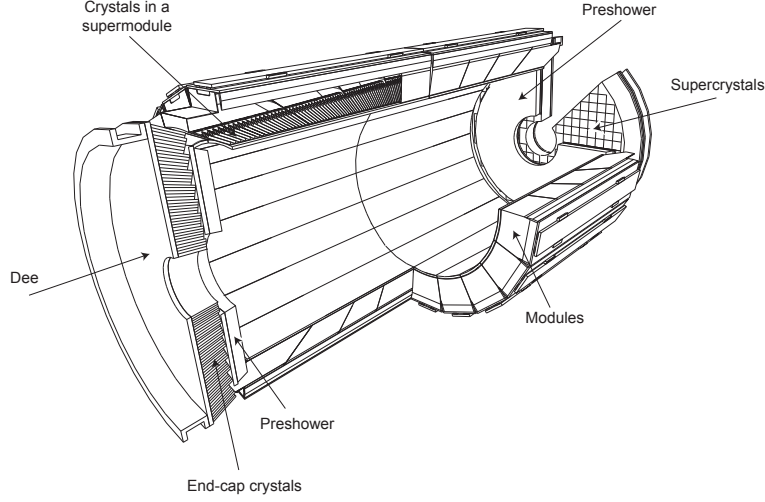
Figure 2.5: Schematic layout of the ECAL crystal modules.

are collected in the attached photodetectors per MeV of incident particle energy from the blue-green scintillation light produced in the crystals. EB crystals are glued to avalanche photodiodes (APDs) while EE crystals are read by vacuum phototriodes (VPTs), each specially designed for the CMS ECAL, as shown in Figure 2.6.
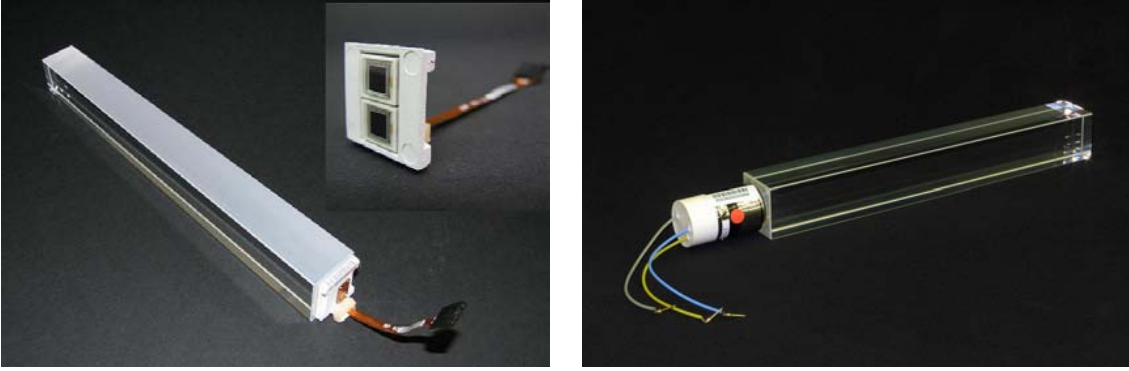

Figure 2.6: EB crystal with one depolished face attached to APD photodetector (left) and EE crystal attached to VPT (right).

The energy resolution of the ECAL depends on the energy of the incident particle, and can be parametrized as the sum of three terms:

$$\left(\frac{\sigma}{E}\right)^2 = \left(\frac{S}{\sqrt{E}}\right)^2 + \left(\frac{N}{E}\right)^2 + C^2 \qquad (2.3)$$

The first term, called the stochastic term, arises from fluctuations in the lateral shower containment, photostatistics, and fluctuations in energy deposited in the preshower de-

tector. The second term, called the noise term, arises from electronic, digitization, and pileup noise. The third term, called the constant term, arises from non-uniformity in light collection, calibration errors, and leakage from the back of the crystals. Test beam experiments using electron beams with momenta 20-250 GeV found approximate values of the parameters: $S = 0.028$, $N = 0.12$, and $C = 0.003$.

2.2.3   Hadronic calorimeter

The hadronic calorimeter (HCAL) lies primarily within the bore of the CMS solenoid, surrounding the ECAL, between 1.77 m and 2.95 m from the beam line, covering up to $|\eta| < 5.2$. The HCAL is divided into four subsystems, shown schematically in Figure 2.7, the barrel region (HB), covering $|\eta| < 1.3$, the endcaps (HE), covering $1.3 < |\eta| < 3$, the outer calorimeter (HO), or tail catcher, double covering the EB and HB regions to ensure complete shower absorption, outside the solenoid, and the forward calorimeter (HF), covering up to $|\eta| < 5.2$ at 11.2 m from the IP. The primary function of the HCAL is to measure the energy and direction of hadronic jets, showers of particles produced from particles composed of quarks and gluons interacting with the detector material. Another important function is to contribute to the measurement of the missing transverse energy (MET), essential for the search for DM done in this analysis, which escapes the detector resulting in large MET.

The HCAL subsystems consist of layers of absorber material and scintillator material, the former causing incident hadrons to shower into quarks and gluons, whose energy is deposited and read out from the latter. Tiles of scintillator material are organized into units called trays. The HB consists of two half-barrels, each with 18 identical ϕ-wedges, each consisting of 17 layers of scintillator material, with each layer containing 108 trays. The scintillator layers are separated by eight 50.5 mm thick and six 56.5 mm thick brass plates and surrounded by an inner 40 mm thick and outer 75 mm thick steel plate. The HE disks consist of 36 identical ϕ-wedges, with a total of 1368 trays of 20916 trapezoidal scintillator tiles divided into 18 layers, alternating with 79 mm thick brass plates. The HO layers are each divided into 12 ϕ-sectors, consist of 40 mm thick detector layers of scintillator and aluminum supports, layered into the 75 mm thick steel beams
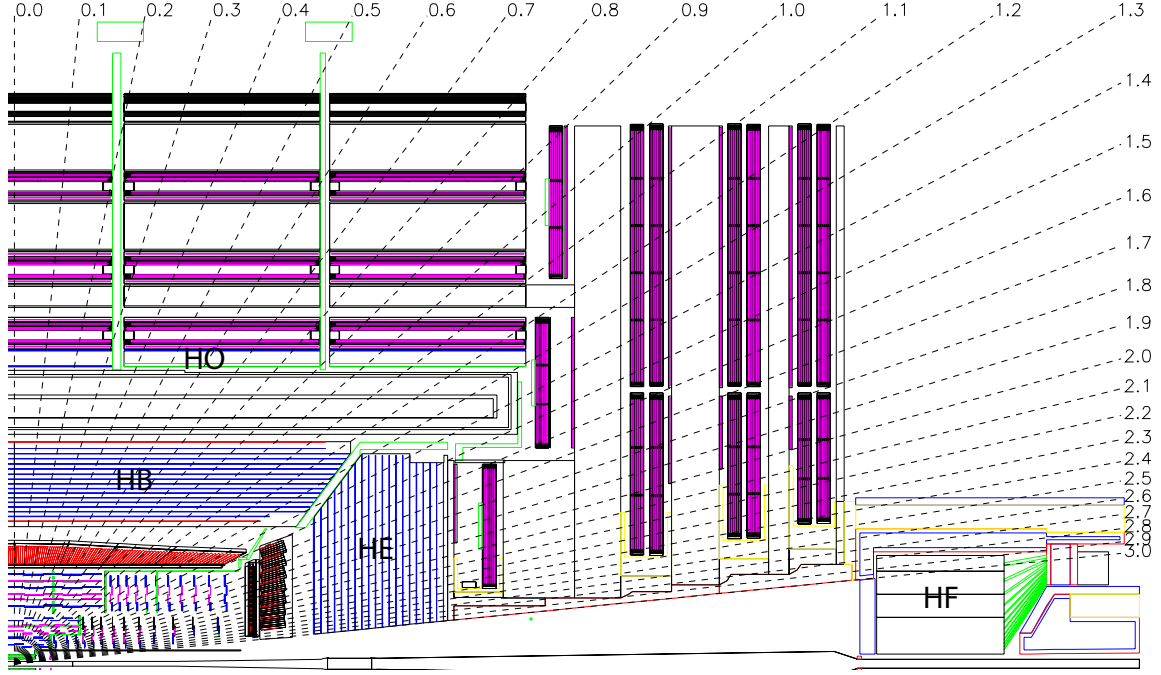
Figure 2.7: Cross sectional view of one quadrant of CMS. The labeled sections are the subsytems of the HCAL, HB, HE, HO, and HF.

of the return yoke. The HB, HE, and HO tiles are arranged to attain a granularity of $(0.087, 0.087)$ in (η, ϕ). The scintillation light produced in the HB, HE, and HO tiles is collected by wavelength-shifting (WLS) fibres, grouped by tray in clear fibres leading to optical decoders which arrange the clear fibers into readout towers, transmitted to hybrid photodiodes (HPD) for amplification and readout. The energy resolution of HB+HE versus HB+HE+HO systems for test beam pions is shown in Figure 2.8, with a clear improvement when including the HO.

The HF barrels consist of eighteen identical ϕ-wedges, with layers of 5 mm thick steel plates. Due to higher radiation doses, quartz fibres are used instead of plastic as in the other HCAL subsystems to produce scintillation light. The quartz fibres lie in grooves cut in the steel plates, with half running the full length of the absorber and half starting 22 cm from the front of the HF barrel. This can be used to classify showers as EM or hadronic, as EM showers deposit most of their energy in the first 22 cm while hadronic showers deposit roughly the same energy throughout the material. Fibres are bundled into towers with a granularity of $(0.175, 0.175)$. The HF is also used to measure the luminosity of the
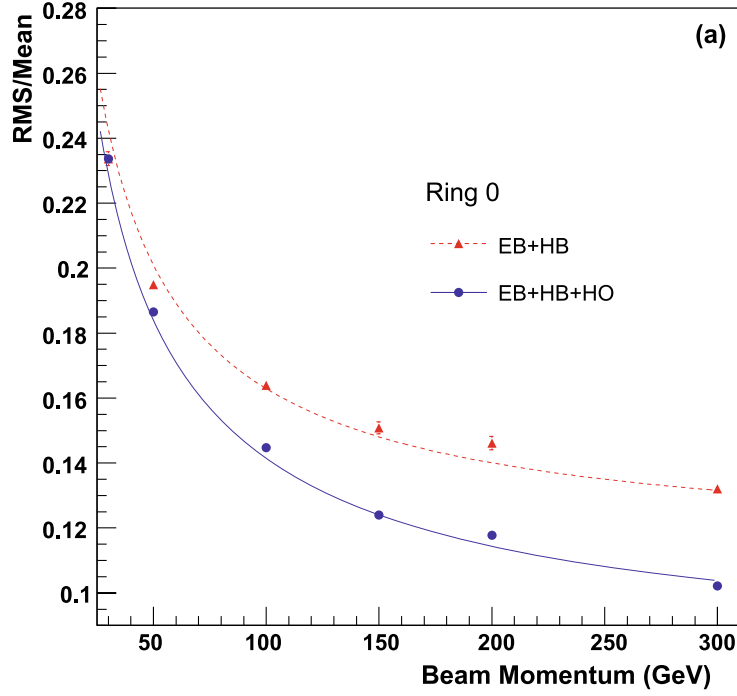
Figure 2.8: Energy resolution of HCAL systems for test beam pions **??**.

LHC beam.

2.2.4   Muon detectors

As muons are able to pass through the inner detector material with little radiative losses, the CMS muon system is the outermost subdetector system, consisting of a barrel region divided into four layers called stations, and endcaps. The barrel region is segmented into regions based on the five 2.536 m yoke rings at $z = 0, \pm 5.342, \pm 2.686$ and the iron ribs of the yoke support structure. With the goal of reconstructing the momenta and charge of muons over a wide angular and kinematic range, three types of gas-ionization detection mechanisms are employed: drift tubes (DTs), cathode strip chambers (CSCs), and resistive plate chambers (RPCs).

The barrel DT system consists of drift cells, 13 mm by 42 mm by 2.4 m chambers filled with 85% Argon, 15% CO_2 gas, with outer cathode strips and an inner anode wire to read out charge carriers ionized from the gas when a charge particle passes through. Four drift cells are stacked, staggered by half a cell, to form superlayers (SLs). SLs are combined in groups of 2-3 for form drift chambers. The inner three stations have 60

DT chambers, with cells having anode wires running in the r-ϕ and z directions. The outer station has 70 DT chambers with cells having anode wires running only in the r-ϕ direction. A schematic diagram of the layout of the DT chambers, layered in the iron yoke, is shown if Figure 2.9.
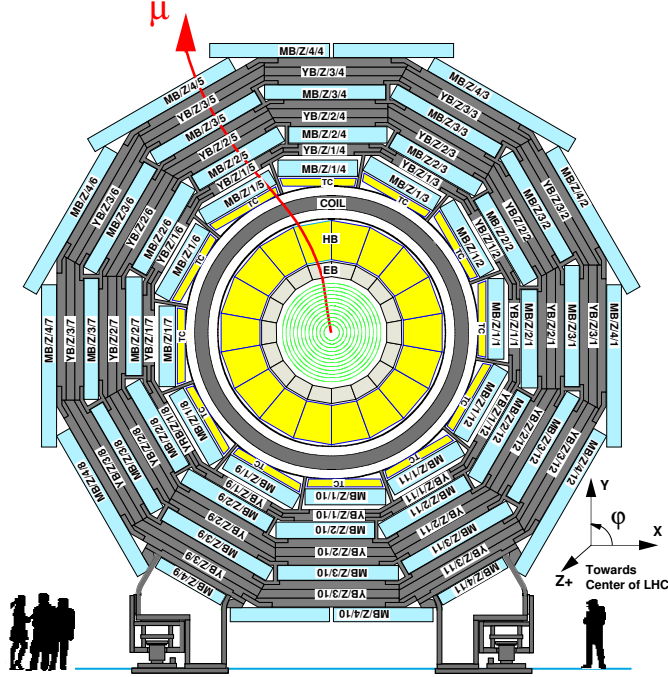

Figure 2.9: Schematic diagram showing DT chambers in light blue.

The endcap CSC system consists of 468 trapezoidal CSC modules, proportional counters with six azimuthal anode wires running perpendicular to seven radial cathode strips, providing measurements of r and ϕ with 80μm resolution with pseudorapidity coverage $0.9 < |\eta| < 2.4$. Muons passing though the chambers' 40%:50%:10%, Ar:CO_2:CF_4 gas mixture produce an avalanche of positive charge carriers, whose signals are interpolated across multiple cathode strips along the anode wires to reconstruct the avalanche position. The position of the CSCs in a cutout quadrant of CMS is shown in Figure 2.10.

The final muon subsystem, the 480 rectangular barrel and trapezoidal endcap RPCs, are arranged in six barrel layers, two in stations one and two, and one each in stations three and four, and in three layers in each endcap. The RPC modules contain parallel-plate detectors with 2-3 double gap modules of up to 96 (32) strips, parallel (radial) to the
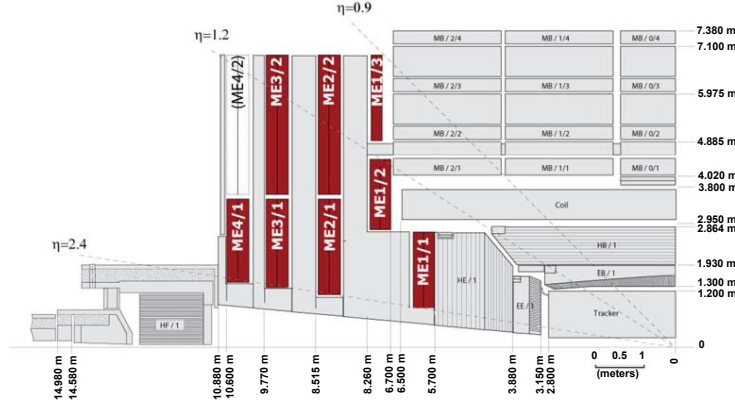
Figure 2.10: Schematic diagram showing CSC locations in red in a quadrant cutout of CMS.

beam line in the barrel (endcap) sections, which collect ionized charge carriers from the 96.2%:3.5%:0.3%, $C_2H_2F_4$:C_4H_{10}:SF_6 gas. A schematic of the module layout is shown in Figure 2.11. The timescale in which RPCs can tag events is faster than the 25 ns bunch crossing time of the LHC, which in combination with the other muon systems, allows efficient triggering on muon events, discussed further in the next section.
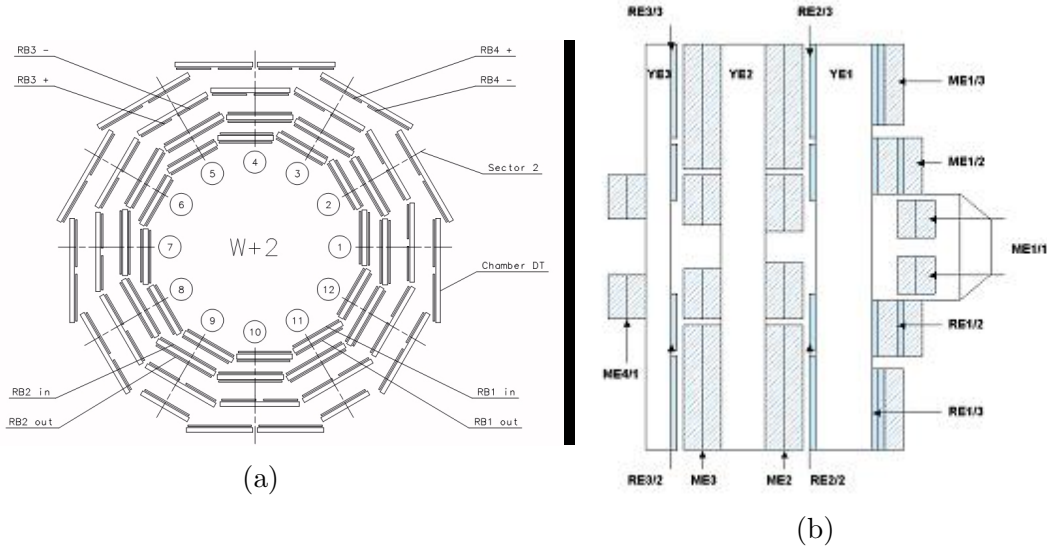

(a)

(b)

Figure 2.11: Schematic diagram showing barrel RPC locations (left) and endcap RPCs (right) in a cross sectional cutout of CMS.

The objective of the muon system to accurately measure the momenta of muons over a wide pseudorapidity range is accomplished, as shown by the transverse momentum
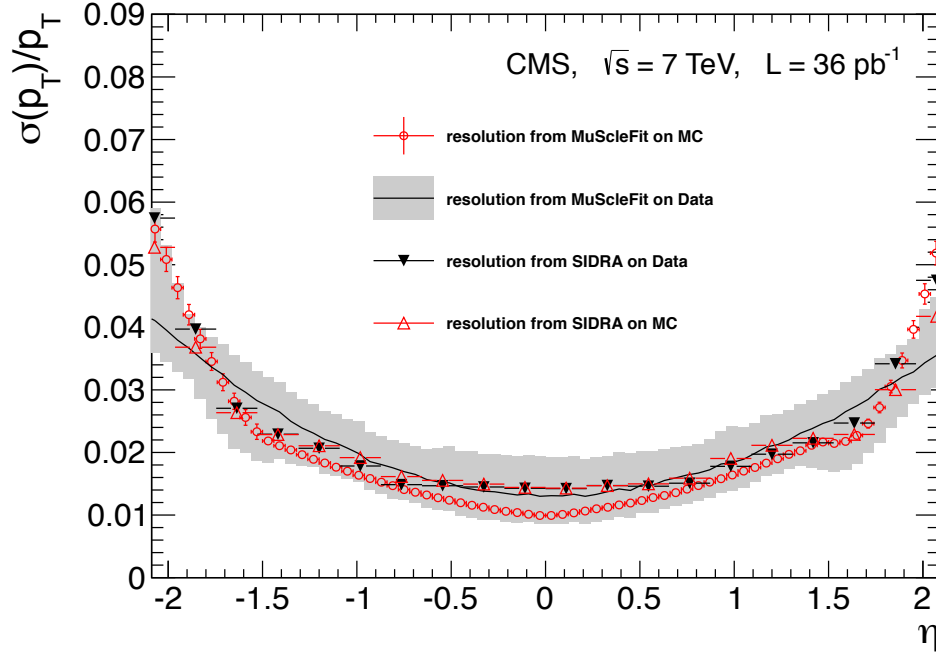
resolution in Figure 2.12, being less than 6% **??**.

Figure 2.12: Transverse momentum resolution versus pseudorapidity for muons from Z decays.

2.2.5   Trigger

In order to reduce the O(100) MHz interaction rate from LHC proton collisions to a computationally managable O(100) kHz rate, a trigger system consisting of an Level-1 Trigger (L1T) and a High-Level Trigger (HLT), is employed. The L1T, summarized in Figure 2.13, uses mainly FPGA technology on the front-end electronics to compile local trigger primitives from calorimeter towers and muon tracks into regional triggers, which use pattern logic to identify objects like electrons/muons. The highest quality objects are piped to the global trigger, which decides, based on further calculations and input on the status of the sub-detectors, whether an event is rejected, or an L1 Accept signal is sent to the Timing, Trigger, and Control (TTC) system for reading out the front-end data buffers, with a latency of 3.2 μs.

After an event passes the L1T, the entire event data is read out by the data acquisition (DAQ) system, summarized in Figure **??**. First, data is read out from the subdetector front-end buffers to the front-end drivers (FEDs), followed by the merging of FED frag-
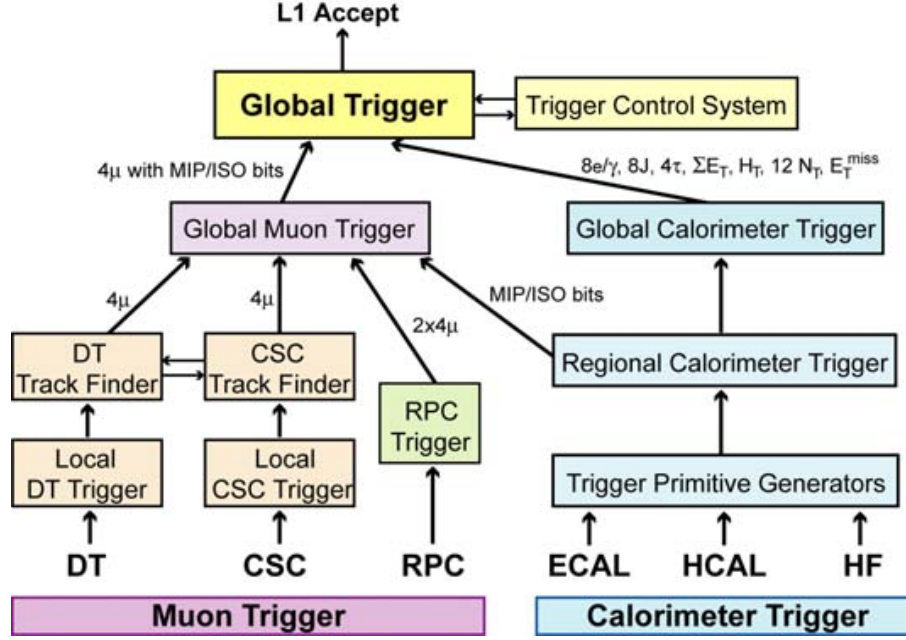
Figure 2.13: .

ments by the Event Builder and the submission of the complete event data to the HLT by the Event Filter. The HLT is a software system, which uses filtering and reconstruction algorithms to select events based on their physics object content, with different paths based on the different combinations of objects used in physics analyses. The HLT paths used in this analysis are based on combinations of high quality lepton objects, such as two muons or two electrons, and are discussed further in the next chapter. Data quality monitoring (DQM), is also carried out at this step, to ensure all subsystems are behaving properly and the data being collected is usable for analysis. Data passing the HLT is saved to storage and processed in the offline software system before being provided to analyzers for physics searches.

In order to verify that the live trigger system is performing as expected and to emulate the trigger system for the production of simulated events, an offline trigger software framework is developed and maintained in parallel with the hardware system. For each calorimeter and muon trigger subsystem, there is a corresponding software emulator that simulates the hardware decisions. The live DQM system used by trigger shifters compares the hardware output to the output of the emulators. In addition to DQM, the trigger
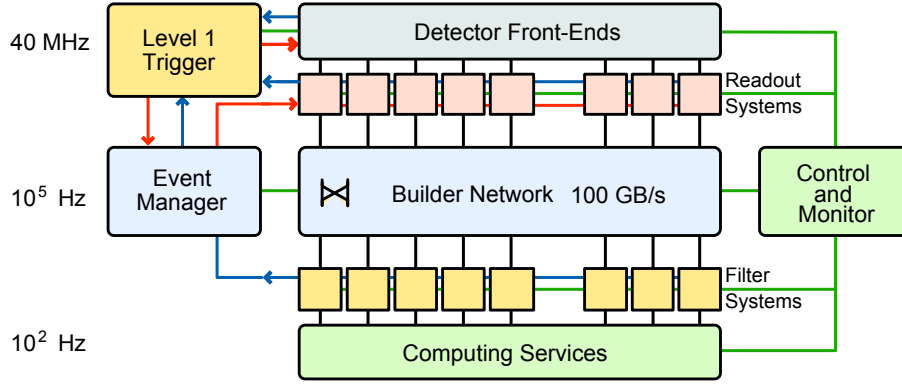
Figure 2.14: .

software framework is used to calculate the L1T efficiencies, or the efficiency of detection for various reconstructed physics objects. The service work conducted in the process of completing this thesis consisted of contributing to the upgrade of the offline software to be based on calorimeter Layers instead of the regional (RCT) and global trigger (GCT) sub-systems of the Run 1 legacy format described above, and the development of automated workflows for trigger DQM. The Run 2 calorimeter trigger system is based on two layers, Layer1, responsible for constructing towers from the energy deposits in ECAL and HCAL modules, and Layer2, which algorithmically builds physics objects from Layer1 towers. A staggered upgrade plan was carried out with the GCT replaced by Layer2 in 2015 (called Stage1) and the RCT to Layer1 in 2016 (called Stage2). During partial upgrades, data formats would be upconverted or downconverted before or after an upgrade stage where applicable to keep the entire workflow working.

Chapter 3

Event reconstruction and simulation

This chapter overviews the algorithms used to reconstruct the trajectories and identify (ID) types of particles produced in proton-proton collisions in CMS, collectively known as Particle Flow (PF), and how these collisions are simulated. Unless otherwise noted, the material in the first section comes from reference **??**.

3.1   Particle reconstruction

The PF algorithms combine information from all of the CMS sub-detectors discussed in the previous chapter to reconstruct the particles produced in the collision event. Since many of the particles produced initially in the collision are unstable, decaying before they have time to interact with the sub-detectors, PF reconstructs the stable particles: electrons, muons, photons, and hadrons. The remaining physics objects of interest, jets, missing energy, taus, etc, can be determined from the information provided by the stable PF-IDed particles.

The different particles are reconstructed and IDed using information from individual sub-detectors, or combinations of sub-detectors. The direction and momentum of charged particles is measured by the tracker. Electrons are reconstructed using tracks and energy deposits in the ECAL. Muons are reconstructed from a combination of tracker and muon chamber data. Photons are reconstructed from energy deposits in the ECAL. Finally, charged and neutral hadrons are reconstructed from energy deposited primarily in the HCAL, with a contribution from energy deposits in the ECAL. The missing transverse

energy, an observable of particular importance to this analysis, used to identify DM that does not interact with the detector material, is the modulus of the sum of transverse momenta of all the PF reconstructed particles.

The basic pieces of information from the subdetectors used by PF are called elements, and consist of charged-particle tracks, muon tracks, and calorimeter clusters. The tracker provides charged-particle track elements. Since the tracker has the best momentum resolution of the subdetectors, it is of critical importance that the tracking efficiency be nearly 100%, with as low a fake rate as possible, to reduce an excess in reconstructed energy. These two goals are accomplished using an iterative algorithm: first, tracks are seeded using very tight criteria, yielding a low efficiency, but negligible fake rate, then track seed criteria are loosened and hits that clearly belong to a track are removed, resulting in increasing efficiency. The ECAL and HCAL subsystems (ECAL barrel, HCAL barrel, HCAL endcap, PS first layer, and PS second layer) provide cluster elements. The calorimeter clustering algorithm measures the energy and direction of neutral particles (e.g. photons, neutral hadrons), differentiates energy deposits from neutral and charged hadrons, reconstructs electrons, and contributes to the reconstruction of charged hadrons. The algorithm is summarized as follows: cluster seeds are identified as energy deposit peaks over a given energy, from which topological clusters are grown by appending adjacent cells, and last, topological clusters seed PF clusters. An example is shown in Figure 3.1, where a simple jet is reconstructed into four clusters, shown as dots.

Once the PF elements are determined, they are linked together into blocks, which correspond to the signatures left in the sub-detectors of a single particle. Single particles typically leave one to three elements. The linking algorithm determines the quality of the link between all pairwise elements in an event, then forms blocks from the highest quality links, starting from the tracker, and proceeding outward through the calorimeters and muon chambers. Once the blocks are formed, PF associates a global event particle with each block. PF muons are formed from global muon candidates if its momentum is consistent across all track elements. PF electrons are IDed from electron candidates using tracker and ECAL cluster variables, accounting for the Bremsstrahlung photons produced

when the electron passes through the tracker material. Once the elements associated to PF muons and PF electrons are removed, the remaining elements are analyzed to ID charged hadrons, photons, or neutral hadrons. PF charged hadrons are associated to remaining tracks if the linked clusters are consistent with the measured momenta. If the energy of the linked clusters is much larger than the track momentum, accounting for uncertainties, a PF photon or PF neutral hadron is formed. Any remaning clusters without linked tracks form PF photons or PF neutral hadrons.

As previously discussed, once the PF particles are identified, additional information about the event can be inferred. A quantity of particular importance to this analysis is the missing transverse energy (MET), defined above. The performance of the PF algorithms determination of the MET is shown in Figure 3.2 by the resolution of PF measured MET as a function of the true MET to be within $\pm 5\%$ above 20 GeV.

3.2   Monte Carlo event simulation

The simulation of proton collision events and their detection using Monte Carlo (MC) techniques is useful for several purposes. In addition to using the simulated events to test the detector hardware and software performance without collecting true data, simulations are used to build background models when searching the data for new physics processes. New physics signatures usually appear as excesses in data above a SM background. The background model consists of SM processes which produce the same or similar signature as the new signal being searched for. These processes are modelled either using purely simulated events, or a combination of simulated events and data-driven techniques. In either case, it is often necessary to weight the background events by correction scale factors measured using data, which account for shortcomings of the simulations, such as the inability to perform perturbative QCD calculations for low momentum transfer processes. MC event generation can be factored into two parts: modeling the initial particles produced in a collision event and modeling how these initial particles evolve in and interact with the detector.

The first part of MC event generation is modeling the proton-proton collision and the

initial particles produced at the primary vertex. Several software packages are used by CMS analysts to generate collision events and calculate the cross sections of the simulated processes, including PYTHIA **??**, MADGRAPH **??**, BlackHat and Sherpa **??**, and POWHEG **??**. The packages have different implementations, but the underlying principles are the same. The momenta of the proton partons (quarks and gluons) that interact in the initial scatter are determined probabilistically by random sampling from the parton distribution functions (PDFs), which give the probability that a parton will carry a fraction x of the proton momentum. This is straightforward for processes with two incoming and one outgoing particle $(2 \rightarrow 1)$ and two incoming and two outgoing particles $(2 \rightarrow 2)$, in which the outcomes are weighted by their relative cross sections and determined probabalistically. For radiative processes such as ISR and FSR of a photon or gluon, generally $1 \rightarrow 2$ processes, higher order matrix elements must be calculated or approximated. Once the initial particles are determined, their fragmentation and decays are simulated in a process called hadronization, until the final stable particles are produced.

The second part of MC event generation is simulating the detector response to the stable particles produced in the first step, including their interaction with the detector material itself, both active elements and structural material. The primary software package used in this step by CMS is GEANT **??**, in which a complete digital representation of the CMS detector is built. GEANT simulates the passage of each each stable particle, step-by-step, outward through the detector, probabilistically determining the interaction that occurs at each step depending on the particle's energy, material it is in, and the EM field present. Since the detector is not perfectly efficienct, both because the acceptance is less than one and the reconstruction efficiency of the individual detector elements is suboptimal, calibration values must be measured at CMS and fed back in to the simulations, so that the performance of the detector can be accurately simulated. Once the final response of the detector is simulated, the resulting MC may be weighted by scale factors measured using real data, in order to correct for mismodelling of the detector.
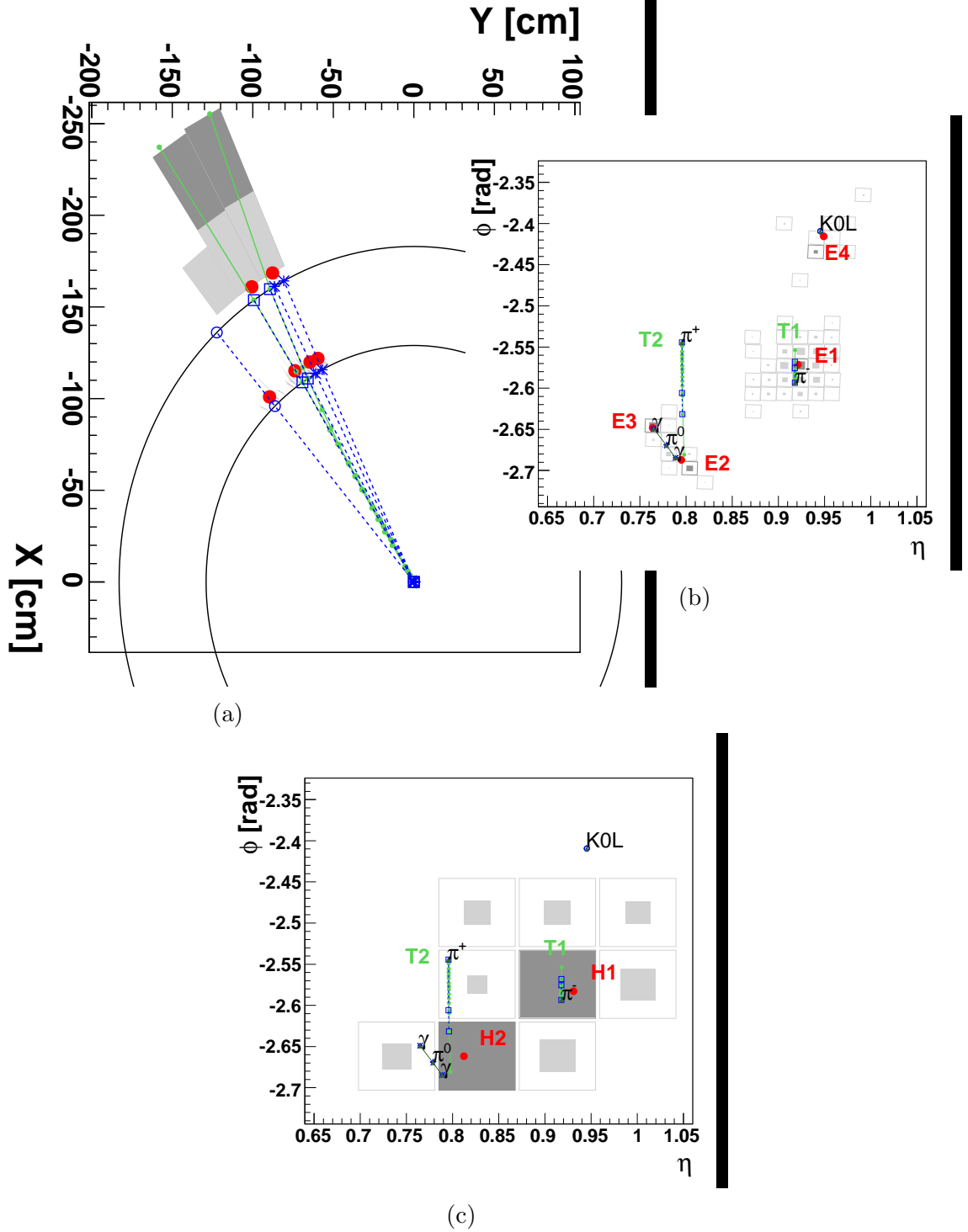
Figure 3.1: Event display of hadronic jet in the x-y plane (a), with solid arcs at the ECAL and HCAL surfaces, and the $\eta - \phi$ plane for the ECAL (b) and HCAL (c). The locations of clusters are given by the solid dots.
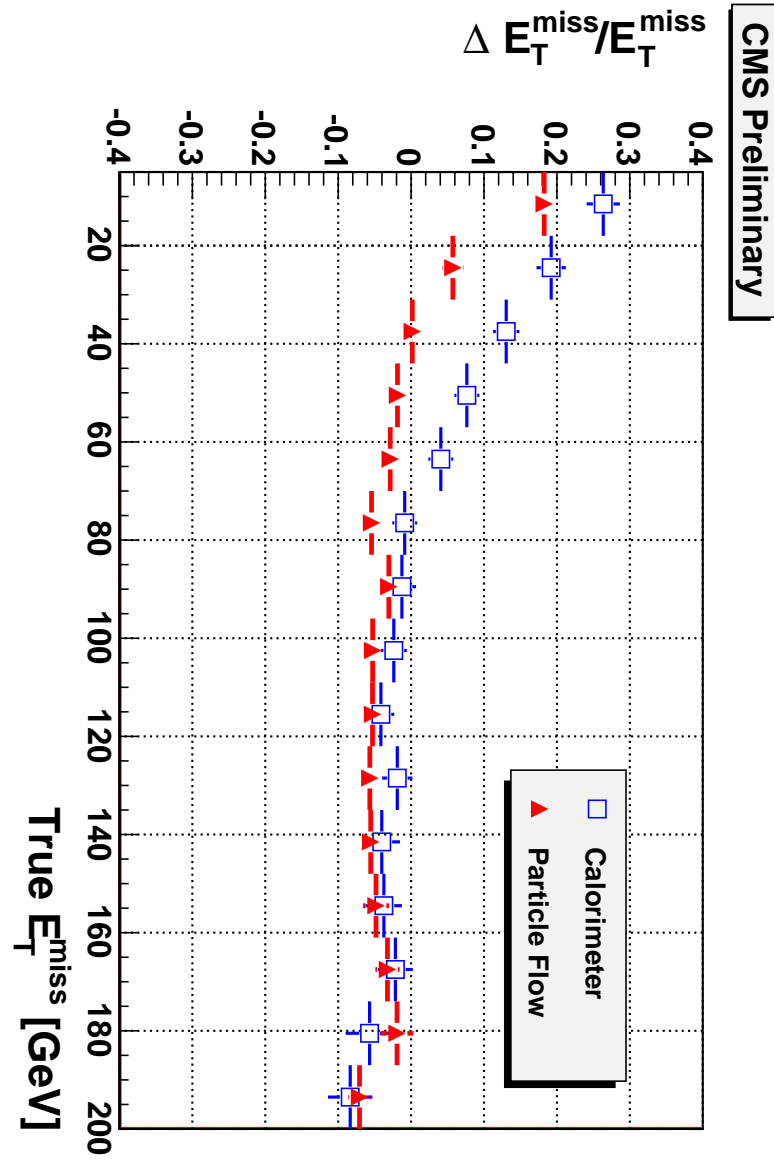
Figure 3.2: MET reconstruction resolution.

Dustin Ray Burns

June 2017

Physics

A Collider Search for Dark Matter Produced in Association

with a Higgs Boson with the CMS Detector at the 13 TeV LHC

Abstract

The abstract that is submitted to UMI must be formatted as shown in the example here. The body of the abstract cannot exceed 350 words. It should be in typewritten form, double-spaced, and on bond paper. It is important to write an abstract that gives a clear description of the content and major divisions of the dissertation, since UMI will publish the abstract exactly as submitted. Students completing their requirements under Plan A should provide extra copies of the typed summary for use by the dissertation committee during the examination.

The abstract that is submitted to UMI must be formatted as shown in the example here. The body of the abstract cannot exceed 350 words. It should be in typewritten form, double-spaced, and on bond paper. It is important to write an abstract that gives a clear description of the content and major divisions of the dissertation, since UMI will publish the abstract exactly as submitted. Students completing their requirements under Plan A should provide extra copies of the typed summary for use by the dissertation committee during the examination.